



# Experimental Characterization of an Axisymmetric Transonic Separated Flow for Computational Fluid Dynamics Validation

Kyle P. Lynch,\* Blake W. Lance,<sup>†</sup> Nathan E. Miller,<sup>‡</sup> Matthew F. Barone,<sup>§</sup> and Steven J. Beresh<sup>¶</sup>  
*Sandia National Laboratories, Albuquerque, New Mexico 87123*

<https://doi.org/10.2514/1.J062278>

An experimental characterization of transonic, turbulent, separated flow generated by an axisymmetric model is presented, with intent for use as a computational validation case. The model is a scaled version of a geometry inspired by Bachalo and Johnson ("Transonic, Turbulent Boundary-Layer Separation Generated on an Axisymmetric Flow Model," *AIAA Journal*, Vol. 24, No. 3, 1986, pp. 437–442), consisting of a circular bump on a constant-diameter cylinder aligned with the flow. The Mach 0.875 flow is turbulent approaching the bump and becomes locally supersonic at the apex. This leads to a shock-wave/boundary-layer interaction, a separation bubble, and unsteady flow reattachment downstream. Tunnel boundary conditions are characterized, and mean surface pressure, mean skin friction, and both mean and fluctuating velocity fields are measured throughout the interaction region. Uncertainty estimates are provided for all measurements. The degree of flow axisymmetry and evidence of relaminarization are discussed, and a comparison is made to historical data.

## Nomenclature

|                 |   |
|-----------------|---|
| $a$             | = nose length   |
| $a_t$           | = step position   |
| $b$             | = forebody length   |
| $C_f$           | = skin friction coefficient                               |
| $C_p$           | = pressure coefficient                                    |
| $c$             | = bump chord  |
| $c_r$           | = fillet radius coefficient                               |
| $d$             | = cylinder diameter                                       |
| $e$             | = afterbody length  |
| $h$             | = bump height   |
| $I$             | = image intensity   |
| $M$             | = Mach number   |
| $P$             | = pressure  |
| $t$             | = step height   |
| $u$             | = velocity component in the $x$ direction                 |
| $u_e$           | = boundary-layer edge velocity                            |
| $u^+$           | = velocity in the $x$ direction scaled by inner variables |
| $u'$            | = fluctuating velocity component in the $x$ direction     |
| $v$             | = velocity component in the $y$ direction                 |
| $v'$            | = fluctuating velocity component in the $y$ direction     |
| $y^+$           | = position in the $y$ direction scaled by inner variables |
| $\gamma$        | = ratio of specific heats                                 |
| $\Delta t$      | = particle image velocimetry laser pulse time separation  |
| $\delta^*$      | = boundary-layer displacement thickness                   |
| $\delta_\theta$ | = boundary-layer momentum thickness                       |
| $\delta_{99}$   | = boundary-layer 99% thickness                            |
| $\theta$        | = azimuth angle around model                              |

$\theta_i$  = oil-film interferometry light incidence angle

## Subscripts

|     |  |
|-----|--|
| ref | = at reference location of $x/c = 0$                                     |
| 0   | = stagnation conditions or pressure-sensitive paint reference conditions |

## I. Introduction

THE performance of aerospace vehicles is highly dependent on the state of the boundary layer and whether it is attached or separated. The physics of smooth-body turbulent boundary-layer separation is of particular interest because the separation is triggered primarily by flow-induced pressure gradients rather than geometric discontinuities. Shock-wave-induced separation occurs commonly on flight vehicles operating at transonic conditions, with critically important impact on aerodynamic performance. A related topic is complex, coupled flow behavior such as transonic buffet, where shock-induced separation leads to an instability in the shock-wave/boundary-layer interaction, shock oscillation, and large unsteady pressure fluctuations [1,2]. Prediction of these complex flows using Reynolds-averaged Navier-Stokes (RANS), large-eddy simulation (LES), or hybrid RANS-LES approaches remains challenging [3,4]. Therefore, there is continued need for well-characterized data on smooth-body separation for developing improved turbulence models and prediction capabilities.

The need for additional datasets has motivated several recent smooth-body separation experiments at a variety of scales and speed regimes, including the NASA low-speed two-dimensional (2-D) hump model [5], the Notre Dame/NASA Langley backward-facing ramp [6], the Stanford 2-D rounded backstep [7], the Notre Dame/Boeing Speed Bump [8], the NASA FAITH Hill [9], and the Virginia Tech BEVERLI Hill [10]. Common in each are wall-mounted smooth geometries designed to generate nominally uniform spanwise separation (e.g., the backward facing ramp), or highly three-dimensional separation (e.g., the FAITH Hill). Another commonality is the speed range: these experiments are conducted in low-speed, subsonic flow. At transonic speeds, the flow complexity increases as shock waves may be generated, leading to additional localized pressure gradients that affect the boundary layer and separation. Such phenomena are typically studied in the context of transonic buffet using 2-D airfoil geometries, where the emphasis is on the coupling of the shock and separation location and its self-sustained oscillation [1]. It is also studied in airframe integration (NASA Drag Prediction Workshops [11]), where full vehicle models generate spanwise-varying flow separation, often with local, unsteady separation cells. In both scenarios, the separated flow typically does not reattach to the

Received 24 July 2022; revision received 4 November 2022; accepted for publication 29 November 2022; published online 31 January 2023. Copyright © 2022 by the American Institute of Aeronautics and Astronautics, Inc. Under the copyright claimed herein, the U.S. Government has a royalty-free license to exercise all rights for Governmental purposes. All other rights are reserved by the copyright owner. All requests for copying and permission to reprint should be submitted to CCC at www.copyright.com; employ the eISSN 1533-385X to initiate your request. See also AIAA Rights and Permissions www.aiaa.org/randp.

\*Senior Member of the Technical Staff, Aerosciences Department; klynch@sandia.gov. Senior Member AIAA.

<sup>†</sup>Senior Member of the Technical Staff, Verification and Validation, Uncertainty Quantification, Credibility Processes Department. Member AIAA.

<sup>‡</sup>Senior Member of the Technical Staff, Aerosciences Department. Member AIAA.

<sup>§</sup>Principal Member of the Technical Staff, Aerosciences Department. Associate Fellow AIAA.

<sup>¶</sup>Distinguished Member of the Technical Staff, Aerosciences Department. Associate Fellow AIAA.

surface and these experiments are not well-suited for evaluating the predictive accuracy of reattachment.

A set of experiments was conducted by a team from NASA Ames throughout the late 1970s on an axisymmetric transonic bump [12,13], herein referred to as the Bachalo–Johnson (B-J) experiment. This geometry consisted of an axisymmetric blended circular bump on a cylindrical body aligned with the wind tunnel operating at a high subsonic Mach number, typically between 0.8 and 0.9. A turbulent boundary layer develops along the cylindrical body, which accelerates over the bump. The flow becomes supersonic near the apex of the bump, forming a weak shock that imposes an adverse pressure gradient onto the incoming boundary layer. This causes the boundary layer to separate, forming a separation bubble downstream of the bump, which later undergoes an unsteady reattachment. Intriguingly, experimentally derived mixing lengths show excursions from equilibrium turbulence production and dissipation, suggesting that fixed-parameter turbulence models may be inaccurate in this flow.

The B-J geometry was tested in the NASA Ames 2 ft  $\times$  2 ft and 6 ft  $\times$  6 ft transonic facilities, where measurement systems included surface oil-flow visualization, schlieren/interferometric imaging, surface pressure taps, and a traversing laser-Doppler anemometer. These measurements provided the mean surface pressure coefficient, separation bubble length, mean velocity, and turbulent stresses, and some derived properties such as turbulent mixing length. However, this experiment did not produce data on skin friction, and only limited data on flow unsteadiness, shock location, and higher-order turbulent statistics. An additional omission in the experiment was a detailed characterization of the inflow conditions such as freestream turbulence intensity and the effect of the porous wind tunnel wall. Measurement uncertainty quantification was unaddressed as well. These omissions were later understood to be important elements of a full characterization of experimental conditions for computational validation and model development studies [14]. Regardless, this experiment remains a popular source of validation data because no alternative provides as attractive a data set for the relevant physics at this Mach number.

The axisymmetric bump geometry is attractive as a model validation case for several reasons: first, axisymmetry nominally removes questions related to sidewall interference for an equivalent 2-D wall-mounted geometry; second, the boundary-layer thickness can be carefully controlled by the length of the forebody rather than being fixed by the tunnel walls; finally, the simple geometry eases simulation development. This has led to it being extensively used as a computational validation case, including numerous RANS simulations [15–17], detached eddy simulations, direct numerical simulations [18], and wall-resolved LES [19]. Many RANS models provide a reasonable prediction of surface pressure distribution, with moderate model-to-model variation for this quantity. Most RANS models substantially underpredict the measured Reynolds shear stress, in some cases by over 50%, leading to a distortion in the shape of the separated region and variation in flow topology locations. A Reynolds stress transport model has provided improved predictions of Reynolds stress profiles, without substantial gain in accuracy for prediction of surface pressure and separation/reattachment points [15]. Furthermore, RANS simulations show large model-to-model variations in skin friction, beginning in the flow acceleration region over the bump and continuing throughout the separation. Initial wall-modeled LES results did not provide improvement over RANS, prompting an attempt at direct numerical simulation (DNS) for the B-J experiment [18]. The experimental results could not be predicted by DNS for all measured quantities, possibly due to issues related to establishment of the upstream boundary layer and/or the required azimuthal extent of the domain, particularly in the separated flow region. Subsequent wall-resolved LES results that addressed these issues provided better agreement with the experiment, although lingering unquantified experimental uncertainties have proved a hindrance to fully conclusive comparisons [19]. The relatively high Reynolds number of the B-J flow has precluded further pursuit of the DNS studies. Further simulation validation studies would benefit from a new experiment that removes the ambiguities found in the

prototypical B-J effort and incorporates modern thought concerning validation experiments [14,20,21].

This study revisits the B-J experiment, with five goals: first, to extend data on surface pressure, velocity field, and turbulent statistics; second, to apply modern diagnostics such as particle image velocimetry (PIV), pressure-sensitive paint (PSP), and oil film interferometry to quantify the velocity field, pressure, and surface shear stress; third, to document the tunnel conditions for use as simulation boundary conditions; fourth, perform uncertainty quantification on reported quantities; and fifth, to run the experiment at a lower Reynolds number that is tractable for DNS. Due to the reduced Reynolds number and different wind tunnel and model configuration, we emphasize that this experiment is not meant to be an exact replica of B-J, but a standalone, separate experiment containing similar flow physics and specifically designed as a validation data set.

The paper is organized as follows. Section II describes experimental design, including model and tunnel details and information on each diagnostic. In Sec. III, results are presented, consisting of tunnel conditions and flow over the bump. Section IV provides more detailed discussion of the results to highlight specific flow characteristics and provide a comparison to the classic B-J data.

## II. Experiment Design

### A. Tunnel and Flow Model

The experiment was conducted in the Trisonic Wind Tunnel (TWT) at Sandia National Laboratories (SNL). The TWT is a blow-down-to-atmosphere facility using air as the test gas with interchangeable test sections and nozzles. Using a converging nozzle, it can achieve Mach numbers from 0.5 to 1.3 using a variable downstream choke. The test section is a constant-area rectangular duct of dimensions 30.5 cm  $\times$  30.5 cm enclosed within a plenum to accommodate ventilated test section configurations. The TWT has a run time of 30–45 s with 20–30 min between runs. The stagnation pressure can be varied between approximately 110 and 240 kPa, and reservoir heating maintains a stagnation temperature of approximately 38–49°C during each run. Transonic testing is typically conducted using a ventilated, porous wall configuration; however, solid walls were chosen to provide a simplified boundary condition for simulations. This restricts the model scale due to tunnel blockage as discussed below. Details of the wind tunnel geometry, including scripts to generate the tunnel wall contour, are included here as supplemental material and on the NASA turbulence modeling resource [15]. Historical measurements of the tunnel using five-hole probes showed a flow angularity of approximately 0.35 deg, and centerline flow nonuniformity of approximately 0.5% of the free-stream value [22]. The tunnel has closed-loop control of stagnation pressure, but fixed choke position; this leads to minor variations in Mach number between runs that will be characterized in Sec. III.

The TWT is smaller than the NASA Ames 6 ft  $\times$  6 ft and 2 ft  $\times$  2 ft tunnels used by Bachalo and Johnson. The reduced scale of the wind tunnel and use of solid walls requires a scaled-down model. Further, there are geometric ambiguities in the model definition regarding the intersection of the bump with the Bachalo and Johnson model [19]. Therefore, an analytical definition of the geometry was produced; a schematic is given in Fig. 1. A cylindrical body of diameter  $d$  is capped by an elliptical nose of length  $a$ . The elliptical nose was chosen for suitability in a high subsonic freestream and smooth transition to the forebody. At location  $a_t$ , a backward-facing step of height  $t$  fixes the laminar-turbulent transition location.

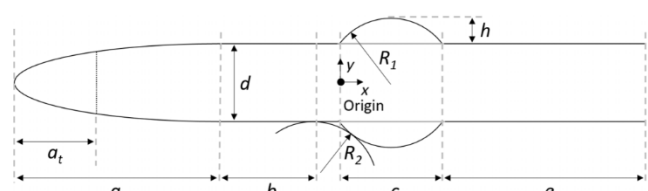


**Fig. 1 Schematic diagram of model (not to scale). Flow is from left to right. Detailed values provided in Table 1.**

**Table 1 Geometry parameters for the model**

| Parameter                        | Value     |
|----------------------------------|-----------|
| Nose length, $a$                 | 5.0 in.   |
| Forebody length, $b$             | 4.0 in.   |
| Cylinder diameter, $d$           | 1.9 in.   |
| Step height, $t$                 | 0.005 in. |
| Step position, $a_s$             | 3.0 in.   |
| Bump chord, $c$                  | 2.53 in.  |
| Bump height, $h$                 | 0.24 in.  |
| Fillet radius coefficient, $c_f$ | 1.2       |
| Afterbody length, $e$            | 12.0 in.  |

Following the nose is a constant-diameter forebody of length  $b$ . The bump is defined as a circular section of radius  $R_1$  and chord  $c$ . It intersects the forebody using a circular fillet of radius  $R_2 = c_f R_1$  tangent to both the forebody and bump. The bump intersects a constant-diameter afterbody with no fillet, and the afterbody, with length  $e$ , continues the geometry to the sting mount of the wind tunnel. The apex of the bump is height  $h$  above the constant-diameter fore/afterbody.

Two geometric ratios from the B-J experiment were maintained: the bump height-to-diameter ratio,  $h/d = 1/8$ , and the chord-to-diameter ratio,  $c/d = 4/3$ . Additionally, the ratio of boundary-layer thickness to bump height was maintained at 0.5 by adjusting the forebody length and estimating using a flat-plate turbulent boundary-layer correlation. The free parameter  $d$  was set to the largest value possible while still providing an enough area ratio for the tunnel to start at Mach 0.875. The parameter values are provided in Table 1; scripts to generate the model profile are provided as supplemental material and on the NASA Turbulence Modeling Resource [15]. Two models were built: first, a black anodized model for velocimetry and oil-flow visualization, and second, an instrumented, polished aluminum model for PSP and oil-film interferometry. Both models were machined from 7075-T6 aluminum. The models were sting mounted on a pitching mechanism; for all runs, the model was positioned at 0 deg angle of attack, verified based on constant distance from the tunnel walls and bubble levels.

## B. Tunnel Pressure and Temperature

The mean static pressure distribution along the center of one test section wall, at locations on the model surface, and the stagnation pressure were measured using a 64-port electronic pressure scanner (Kulite KMP-1-64). The unit consists of 32 ports with a 5 psid

range, 16 ports with 25 psid range, and 16 ports with 15 psia range. The total bias uncertainty of each port is 0.1% of the full-scale value. Data were read directly using a digital readout over Ethernet. The 32 static pressure taps along the test section wall were connected to the 5 psid range. Two taps in the top and bottom of the stagnation chamber were connected to the 25 psid range, as well as model-mounted pressure taps. The reference pressure was plumbed to atmosphere and was simultaneously measured using one port of 15 psia range. Stagnation temperatures were measured using two type-T thermocouples and an NI-9212 module. Model temperature was measured using two Medtherm type-T coaxial thermocouples embedded in the surface of the model and a separate NI-9212 module.

## C. Particle Image Velocimetry

Two-dimensional planar PIV was used to characterize the velocity in multiple regions in the flow. A schematic of the arrangement is given in Fig. 2. Multiple fields of view (FOV) were used: a model-wall (MW FOV) for measuring the incoming boundary-layer thickness; a tunnel-wall (TW FOV) for measuring the test section wall-boundary-layer thickness; a freestream FOV for measuring turbulence intensity (TI FOV), and seven FOV for measuring a high-resolution panorama of the bump and separated flow region (FOV 1–7). For all FOV, common hardware was used: a LaVision Imager scientific complimentary metal-oxide semiconductor (sCMOS) camera ( $2560 \times 2160$  px at 50 Hz,  $6.5 \mu\text{m}$  pixel size) and a Quantel Evergreen HP laser ( $2 \times 310 \text{ mJ/pulse}$  at 25 Hz). Seeding was generated by a Corona Vi-Count 5000 thermal smoke machine, delivering particles approximately  $0.7\text{--}0.8 \mu\text{m}$  diameter as measured in previous tests using a shock-wave test. The laser sheet width was tailored to each FOV size, and the sheet thickness was estimated at 1.0 mm using burn paper.

The small size of the boundary layer upstream of the bump required a high-magnification setup to provide adequate resolution. For the MW FOV, a Nikon 200 mm f/4 Micro-NIKKOR lens and a 2:1 teleconverter provided imaging at 276 px/mm at a working distance of approximately 12 in. The inter-pulse timing  $\Delta t$  was 250 ns, corresponding to a maximum displacement of approximately 20 px. To accommodate the short working distance, the optical setup was “folded” into the tunnel plenum, using a first-surface aluminum mirror to redirect the image to the camera. For the TI FOV, the scale factor was 206 px/mm. FOV 1–7 used the same lens operating at f/8 and with the folded setup, but without the teleconverter to yield a resolution of approximately 122.4 px/mm. The same  $\Delta t$  of 250 ns is used with maximum displacements approximately 12 px. For the TW FOV, the folded setup was retained with a 105 mm lens and yielded a magnification of 0.4 (64 px/mm). Scale calibration was performed using a Thorlabs R2L2S3P3 plate (0.5 mm spacing).

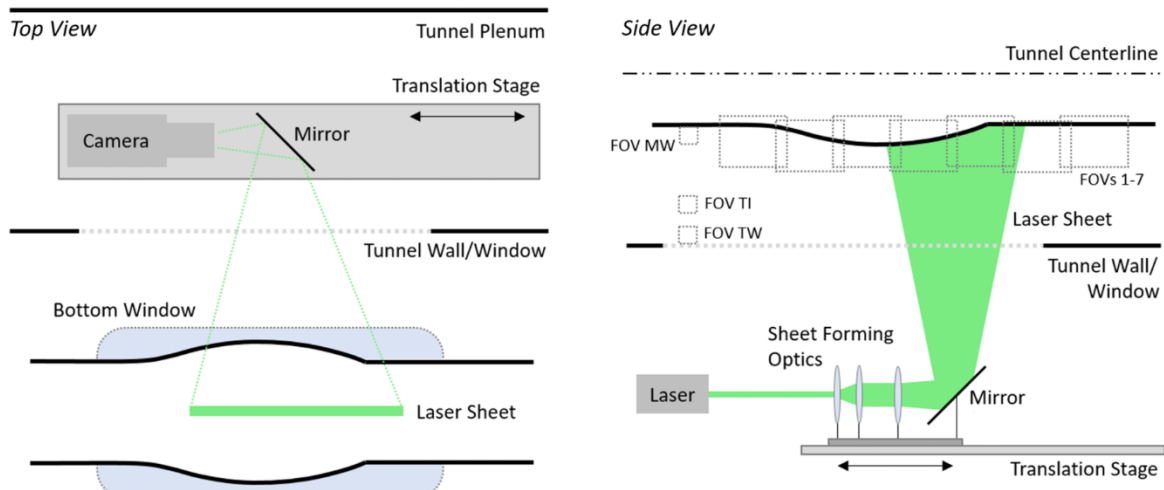


**Fig. 2 Schematic of PIV arrangement. Left, top view showing camera and mirror on translation stage within the tunnel plenum. Right, side view showing laser below tunnel with sheet-forming optics on translation stage. Also shown are the different FOV: MW, model wall; TI, turbulence intensity; TW, tunnel wall; 1–7, panorama of interaction region.**

The relatively high magnifications and tunnel vibrations required shift correction to align the wall interfaces throughout image sequences. Cross-correlation between the first and subsequent images using a large window centered on wall reflections allowed for an integer shift to be calculated and removed. For the MW and TW FOV, the vibration-corrected sequences were analyzed using a sum-of-correlation approach with square 12 px windows (0.04 mm). For the TI FOV, various square window sizes from 256 px (1.2 mm) to 16 px (0.07 mm) were used. For FOV 1–7, a square window size of 32 px (0.26 mm) was used.

The ensemble size for the MW FOV was 3000 independent snapshots assembled from three separate runs. For FOV 1–7, 3500 independent snapshots were acquired. In all processing, Davis 10.1 is used with 75% overlap and Gaussian window weighting. Vector outlier removal was used within the multipass analysis, but not used for the final output. Statistics were calculated using a multipass approach with an inlier threshold of 3 standard deviations from the mean. This software also computed the uncertainty of the cross-correlation via the correlation statistics method and propagated to the final statistics, such that the total uncertainty represents the random and bias uncertainties [23].

#### D. Oil-Film Interferometry

Surface shear stress was measured via oil-film interferometry (OFI). This technique has been used in various configurations including high-speed compressible flows [24], industrial-scale wind-tunnel facilities [25], the NASA 2-D bump configuration [26] and many others. Compared to other shear-stress measurement techniques, the method is relatively simple and inexpensive to implement and can achieve high accuracy. It is particularly well-suited for the current model due to its applicability on curved surfaces, a challenge for discrete shear stress sensors. Further, the measured oil film height is less than 1 micron with height-to-length ratios of 10,000–100,000, ensuring that the method is essentially nonintrusive. OFI uses the thin-oil-film equation to relate the varying height of a patch of oil to the subjected shear stress. The height is measured indirectly using the interference pattern generated by light reflected from a model and the oil interface. Additional details of the technique are given in the overview [27] and derivation of the governing equations in [28].

The optical arrangement is shown in Fig. 3. The model was highly polished using a sequence of automotive rubbing compounds to remove machining marks and ensure uniform reflectivity. Two different light sources were used during different measurement campaigns: first, a mercury-vapor grid lamp (BHK 88-9102-02) placed behind frosted diffuser glass, paired with a 50/50 beamsplitter to orient the illumination along the same light path as the imaging. A Thorlabs FL543.5-10 bandpass filter (center wavelength  $543.5 \pm 2$  nm, full-width half-max  $10 \pm 2$  nm) on the lens selected the 546.1 nm

emission line of the lamp. The low intensity and hazard of working with this lamp motivated switching to a diffuse axial LED (Metaphase MB-DAL-605-B) with built in beam splitter, which is the light source depicted in Fig. 3. No camera filter was required as the LED array emitted at  $470 \pm 10$  nm. The use of different light sources does not affect the results. A PCO edge 5.5 sCMOS camera imaged the oil film at 10 Hz for the entire duration of the run with a 200 mm f-mount lens with the mercury lamp and 105 mm f-mount lens with the LED array, folded using a first-surface aluminum mirror. The camera and lamp were mounted on a translation stage within the tunnel plenum to measure various positions along the model.

Dow Xiameter PMX silicone oil was used. Nominal viscosities of 50, 100, and 200 cSt were selected to enable sufficient oil movement during the run duration. The temperature dependence of viscosity and density for each oil was calibrated using an Anton Paar Stabinger Viscometer. A polynomial fit as a function of temperature to these properties was used as a lookup in the subsequent processing. The oil was applied using a card to create a well-defined leading edge across the observable azimuth and wet the area in the direction of the oil movement. For most runs, a single oil patch was applied on the target section of the model, with some runs applying two patches.

The first step in the image analysis was applying photogrammetry to achieve a mapping between object and image space and retrieve the light incidence angle [29]. The intrinsic camera parameters were estimated by acquiring images of a rigid checkerboard translated and rotated around the measurement volume and analyzing them using the MATLAB camera calibration tool. The extrinsic parameters were estimated using a fiducial fitting procedure: around 60 fiducial marks were machined into the model at 0.5" streamwise increments and 15 deg angular increments, and their positions in the object coordinate system were specified. Note that these marks made a negligible effect on the surface finish of the model. The marks were manually identified in the images, establishing an image-object correspondence. An initial estimate was produced using a perspective-3-point algorithm (MATLAB estimateCameraPose), then refined using a least-squares fit modifying the extrinsic parameters to minimize total reprojection error. The resulting intrinsic and extrinsic parameters defined the object-image mapping, allowing the image data to be unwrapped onto a model-aligned  $x - \theta$  grid. Further, the light incidence angle  $\theta_i$  at each  $x - \theta$  pair was estimated using reflection of the extrinsic translation vector by the local geometry surface normal.

The next step is fringe detection, shown as a series of steps in Fig. 4. The thin-oil-film equation requires integration along a surface flow streamline. Oil-flow visualization showed that these streamlines were found oriented along the  $x$ -axis in all flow regions. For each azimuthal angle, a  $x - t$  diagram of the interferogram was generated for fringe detection. The shear stress gradients on the bump and shock foot region made automated fringe detection challenging; therefore, the peak/valley locations were outlined manually, then refined using an adaptive-window filtering method, which accounted for varying fringe spacing. The refined fringe positions were then converted to a phase offset and height. The height was corrected for the finite leading-edge thickness by using a two-fringe leading-edge intersection extrapolation. The height was integrated to yield the skin friction coefficient via the multi-image method [30], recast in an axisymmetric formulation (personal communication with J. Naughton, Professor at University of Wyoming, March 2021). The time integration in this method used the time-varying values of freestream dynamic pressure and oil viscosity.

Uncertainty analysis in OFI was conducted following [26]. The dominant source was the uncertainty in viscosity arising from the model temperature uncertainty. The time-dependent model temperature uncertainty defined an upper and lower model temperature, which led to an upper and lower bound on viscosity via the oil calibration polynomial fit. These viscosities were separately integrated to yield an upper and lower bound for the skin friction solution for a particular run. The uncertainty introduced from photogrammetry was negligible due to the small light incidence angles. Also accounted for is the random uncertainty, calculated by analyzing the interferograms across different azimuth angles at the same streamwise positions. The typical number of angles was 30. The random uncertainty captured variations caused by camera noise, varying fringe visibility, and artifacts due to dust and

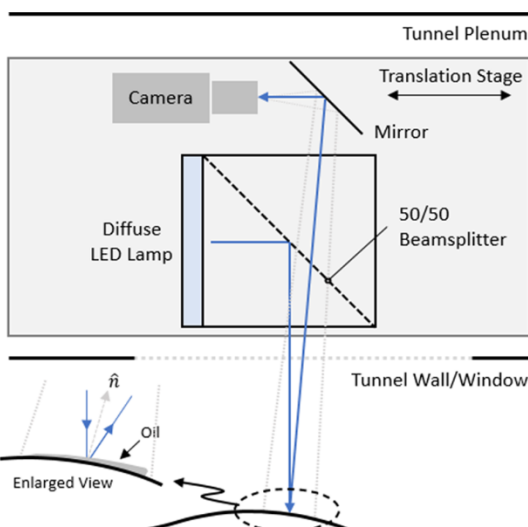


Fig. 3 Schematic of oil-flow interferometry setup.

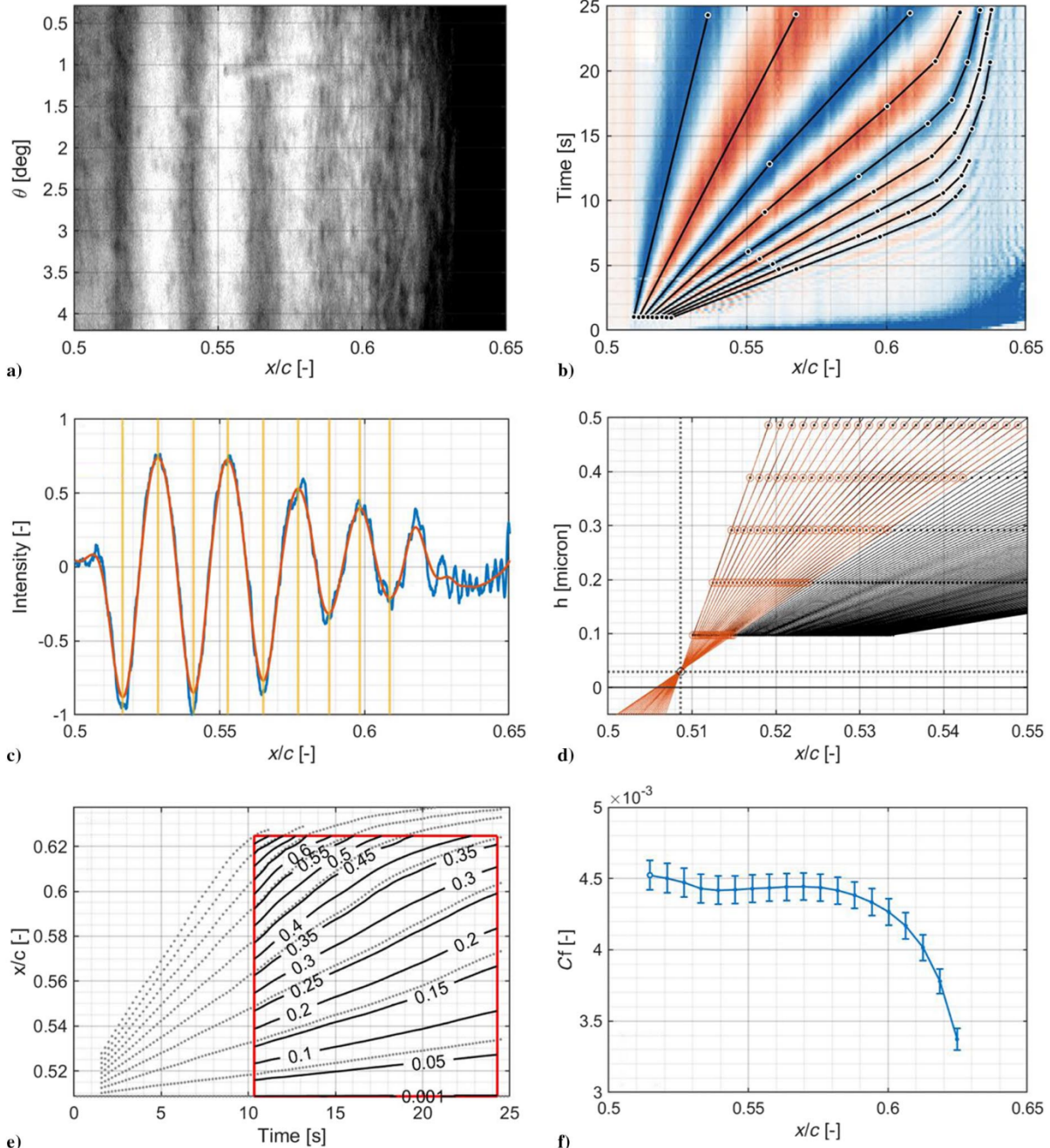


Fig. 4 Steps in the fringe detection and skin friction estimation, example from a run upstream of the shock. a) “Unwrapped” image data halfway through the run; b)  $x-t$  diagram of fringes from a single azimuthal angle; c) fringe detection for one time on the  $x-t$  diagram; d) leading-edge estimation; e) derived height distribution in microns with red box indicating integration bounds; and f) skin friction estimate with uncertainty.

surface imperfections. These sources were considered independent, so the uncertainty was computed as the standard deviation and reported at the 95% confidence level. An additional source of uncertainty is the startup/transient tunnel effects. These were not possible to directly evaluate; however, their effects were minimized by casting the measurement in terms of skin friction coefficient, and ensuring that the tunnel was “on-condition” significantly longer than the startup time of approximately 1 s.

The full description of shear stress along the model is compiled from multiple independent runs, including multiple runs at similar locations. Overlapping data were combined into a single result by bin-averaging and estimating the uncertainty using Student’s  $t$  distribution.

#### E. Pressure-Sensitive Paint

Time-averaged surface pressure was measured using pressure-sensitive paint (PSP). Fluctuating pressures were not measured

because their magnitude was too low for practical measurement. The heated reservoir of the TWT causes a rise in model temperature during the run; therefore, temperature compensating BinaryFIB paint and a FIB Basecoat from ISSI, Inc., were used. The paint contains two dyes that fluoresce at different wavelengths; the first is pressure and temperature sensitive, and the second is temperature sensitive only. Separating and ratioing the signals removes the temperature sensitivity from the measurement. This PSP has a response time of approximately 300 ms, so it is unable to measure unsteady pressure fluctuations along the model with sufficient temporal resolution. Illumination was provided by two ISSI LM2X-DM-400 continuous air-cooled lamps providing 4 W each at 400 nm as depicted in Fig. 5. These were switched on 1 min before running to stabilize the light signal. Two PCO edge 5.5 sCMOS cameras were used with 24 mm f-mount lenses, one equipped with a Midwest Optical Systems 550  $\pm$  10 nm narrowband filter, the other with 650  $\pm$  10 nm. The same

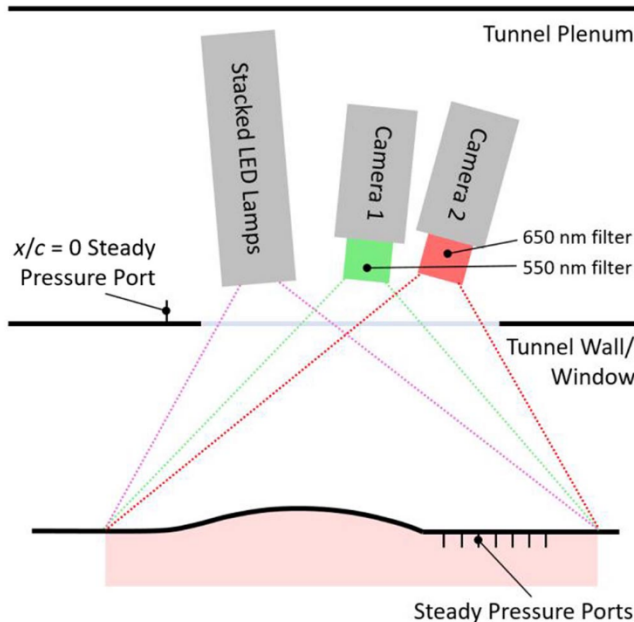


Fig. 5 Schematic of PSP setup.

photogrammetry procedure used in OFI was applied to unwrap the images from the two cameras onto a common model-aligned  $x - \theta$  grid. The ratio is calculated from these gridded data.

An in situ calibration of the PSP was performed using a calibration cell containing a coupon painted and cured simultaneously with the model. The cell was placed in the field of view of the camera, so there were no changes to illumination or imaging compared to the actual runs. The pressure was varied from 0 to 25 psia using a Mensor CP4000 pressure controller (100 psi range, accuracy to 0.02%), with an image acquired at each 1 psi increment, and the 12 psia point was used as the reference pressure. The temperature was held constant at ambient; separate measurements at 150°C temperature showed no change in the resulting fit, which is consistent with the residual low temperature sensitivity of 0.03% per °C reported by the manufacturer for this temperature-compensating paint. The ratio data were least-squares fit using a second-order polynomial  $P/P_0 = f(I_0/I)$ , with uncertainty given by the 95% confidence intervals. The calibration result is shown in Fig. 6 (left). The green dye (G; 550 nm) shows the expected insensitivity to pressure, whereas the red dye (R; 650 nm) is sensitive. Thus, the ratio  $R/G$  is pressure sensitive, with a sensitivity (slope) approaching that of a single-dye PSP (ISSI UniFIB). The increased sensitivity compared to the manufacturer-reported BinaryFIB is due to the use of two cameras with separate color filters, rather than a single camera with Bayer filter used for the manufacturer

calibration. The color overlap in Bayer filters has been shown to reduce the sensitivity of binary PSP paints [31].

An example of the paint response during a run is shown in Fig. 6 (right) at a region upstream of the shock on the bump. An average of images after tunnel shutdown is used as the reference image. The temperature rise of the model causes the green pressure-insensitive camera to show a slow rise in intensity across the run. The red pressure-sensitive camera shows the reduction in intensity corresponding to the below-ambient static pressure in the test section during the run. Ratioing these two channels yields a measurement of approximate constant intensity across the run. The average pressure is calculated using only the data during this constant time, masking the times associated with tunnel startup and shutdown.

The uncertainty analysis in PSP considers calibration uncertainty, temperature sensitivity, camera noise, intrarun variability, and run-to-run variability. The calibration uncertainty is propagated from the 95% confidence intervals of the polynomial fit coefficients (MATLAB *confint* function). The model temperature variation is around 10°C per run, so a conservative estimate of 0.3% uncertainty was used. The effect of camera noise and intrarun variability are considered random noise sources and are evaluated directly from the measurement data via the standard deviation over the multiple images in each run. The uncertainty distribution due to run-to-run variability is estimated via Student's *t*-distribution. Each of these sources is combined via root-sum-of-squares to form the total uncertainty (see the Appendix).

#### F. Oil-Flow Visualization and Schlieren

Surface and flow topology were measured using oil-flow visualization and schlieren imaging, respectively. A fluorescent oil, Magnaflux Zy glo ZP-9F, was illuminated by 400 nm ISSI LM2X-DM-400 lamps and imaged by a FLIR BFLY-PGE-23S6C-C CMOS camera at 10 Hz. Similar photogrammetry procedures as described previously were used to map the images onto a model coordinate system, and topology information was extracted from manual inspection. Schlieren images were acquired using a z-type system with two large-diameter parabolic mirrors, a vertically oriented knife-edge, and a Photron SA-Z camera acquiring at 20 kHz.

### III. Results

#### A. Tunnel Conditions

Multiple runs were required throughout the test campaign, and variations in control valve performance led to variations in the stagnation pressure during each run and between runs. Also, a drift in a control transducer was found between tunnel entries, leading to some runs having a pressure offset. The stagnation pressure time-histories and statistics for all runs were compiled using a histogram approach [32]. The distribution is bimodal due to the transducer drift but is specified by a mean value of 122.0 kPa, and 2.5 and 97.5% percentile

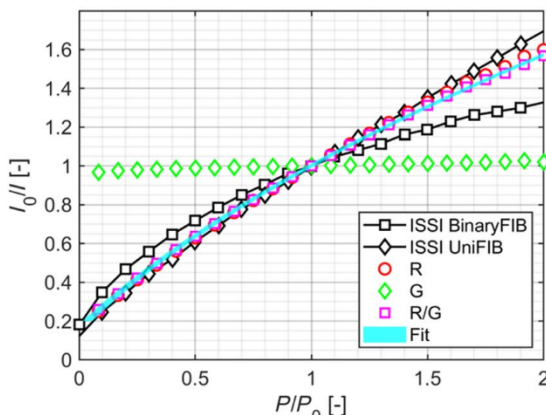
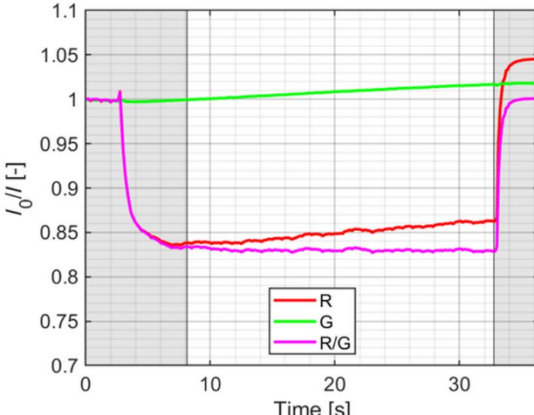


Fig. 6 Left, in situ calibration of the PSP using the calibration cell and ISSI data from the manufacturer. Red and green denote signals from individual cameras, while red/green is the ratio. The calibration fit is given as the cyan line, with dashed lines representing 95% prediction intervals of the fit. Right, example paint response during a run. Shaded areas indicate times masked during statistics calculation.



bounds, suggesting random uncertainties of  $-7.0$  and  $+4.6$  kPa, much larger than the bias uncertainty of  $\pm 0.17$  kPa. In the remainder of the paper, data are analyzed in normalized variables, which reduces the effect of run-to-run variability.

The stagnation temperature also exhibits variation between and during runs due to the constant-volume expansion from the reservoirs as well as the thermal mass of unheated pressure lines between the facility and the heated air reservoirs. It takes roughly 25 s for the temperature to reach a maximum value during a run, after which a decrease in temperature occurs. Variations of up to 10 K occur within a run. The same histogram approach is used, and these percentiles are combined with the bias uncertainty of the thermocouple and DAQ (2.15 K) to yield the reported value of stagnation temperature: 324.4 ( $-9.4, +5.8$ ) K.

The solid wall test section results in a nonuniform pressure distribution along the wall due to model blockage and boundary-layer growth on the model and tunnel walls. This causes the Mach number to increase within the test section (see, e.g., Fig. 6 in [32], included in supplemental material) and is the limiting factor on maximum model size. The nonuniformity makes the definition of a “freestream” or “far-field” flow condition ambiguous. Therefore, a specific definition is provided: reference quantities are defined at the tunnel wall at a streamwise station corresponding to  $x/c = 0$ . Quantities at this location are denoted by the subscript “ref.” The reference Mach number is calculated using isentropic relations based on the tunnel

wall pressure ratio at  $x/c = 0$  and a constant ratio of specific heats,  $\gamma = 1.4$ . The reported value is 0.8747 ( $-0.006, +0.005$ ). The bias uncertainty of the measurement is 0.0017, which was determined by the propagation of pressure ratio to Mach number as given in the Appendix. Note that using a pressure ratio reduces the random uncertainty compared with pressure alone as described previously, but it remains larger than the bias uncertainty as observed here. The reference exit quantities are denoted by the subscript *exit*, corresponding to  $x/c = 6.25$ .

The wind tunnel model increases in temperature during a run due to the elevated stagnation temperature of the tunnel. Variations of up to 10 K occur within a run. Between runs, the model did not fully return to ambient temperature, causing a drift toward warmer model temperatures for subsequent runs. The same histogram approach is taken to quantify the sample distribution, and these percentiles are combined with the bias uncertainty of the thermocouple and DAQ (2.15 K) to yield the reported value of model temperature: 312.6 ( $-10.0, +7.8$ ) K. The larger magnitude of the lower uncertainty is due to the low temperature from the first run of a day, where the model temperature begins at ambient.

The freestream turbulence intensity was measured at  $x/c = 0$  at approximately the midpoint between the model surface and the tunnel wall using the multiple- $\Delta t$  method [33]. This fits a noise propagation model to PIV measurements acquired with different pulse separations,  $\Delta t$ , to extract an unbiased estimate of turbulence intensity in the presence of measurement noise. The model yields a turbulence intensity of 0.23% for a range of window sizes and captures the increase in random noise as the window size is reduced. The uncertainty is estimated at  $\pm 0.01\%$ , based on the variability of the measurement with window size.

The tunnel wall boundary-layer profile as measured using PIV is given in Fig. 7 for cases of an empty tunnel, and with the model installed. For empty tunnel measurements, the tunnel control was modified to maintain the same  $M_{ref}$ . Profiles were extracted at approximately  $x/c = 0$  at the tunnel wall, and a fit was applied for comparison to a canonical compressible turbulent boundary layer [34]. The fit is only applied to points above  $y^+$  of 70, as the Sun and Childs fit does not consider the overlap layer. Further, the high resolution of the measurement did not allow a sufficient measurement extent for direct measurement of the boundary-layer edge velocity  $u_e$ ; thus it was included as an additional fit parameter. The 99% boundary-layer thickness  $\delta_{99}$  is reported as 13.9 mm without the model installed, and 11.8 mm with the model installed. Displacement thicknesses  $\delta^*$  are 2.0 and 1.4 mm, and momentum thicknesses are 1.2 and 1.0 mm, respectively. The boundary-layer thickness is thinner with the model installed due to the increased blockage and the pressure field this imposes on the tunnel wall boundary layer.

The model forebody boundary-layer profile as measured using PIV is given in Fig. 8. Profiles were extracted at  $x/c = -0.78$ , and a fit was applied for comparison to a canonical compressible turbulent

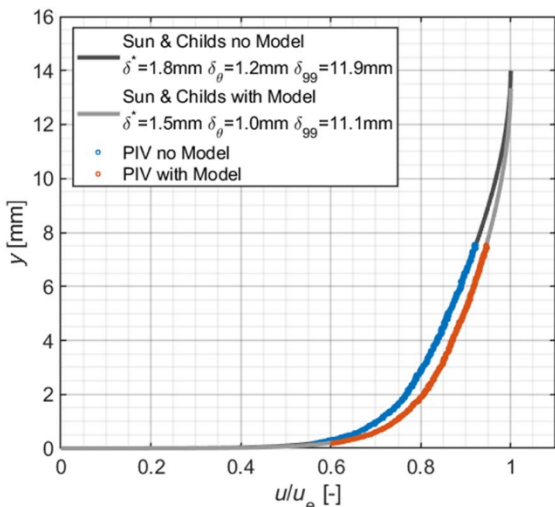


**Fig. 7** Tunnel wall boundary-layer profiles with and without the model installed. Profiles extracted at approximately  $x/c = 0$  at the tunnel wall. Measurement points are given in blue and red; solid lines are fits with the Sun and Childs model [34]. Profiles normalized by respective edge velocities,  $u_e$ .

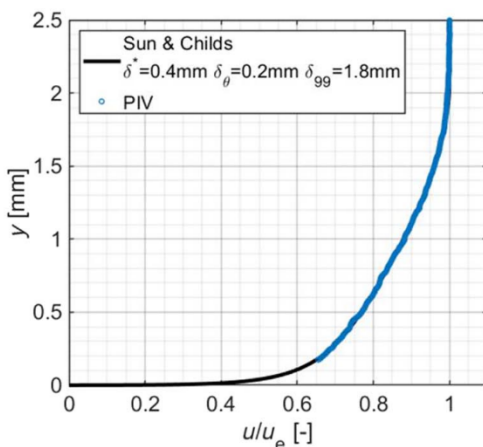


**Fig. 8** Model wall boundary-layer profile. Profiles extracted at approximately  $x/c = -0.78$ . Measurement points given in blue; fit given as solid line [34]. Profiles normalized by edge velocity,  $u_e$ .

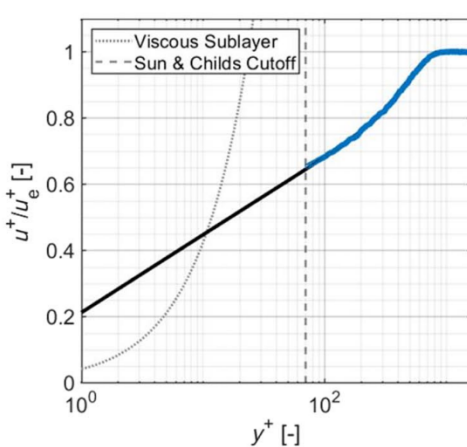


**Fig. 9** Boundary-layer profile on a logarithmic scale. The x-axis is  $y^+ [-]$  on a log scale from  $10^0$  to  $10^2$ . The y-axis is  $u^+/u_e [-]$  from 0 to 1. A blue curve represents PIV measurements, and a black solid line represents the Sun & Childs fit. Two vertical dashed lines indicate the Viscous Sublayer ( $y^+ \approx 30$ ) and the Sun & Childs Cutoff ( $y^+ \approx 70$ ).

**Table 2** Tunnel boundary conditions with mean and lower and upper uncertainty values

| Parameter  | Mean (lower uncertainty value, upper uncertainty value) |
|--|---|
| Stagnation pressure, $p_0$   | 122.0 kPa (-7.0, +4.6 kPa)                              |
| Stagnation temperature, $T_0$  | 324.4 K (-9.4, +5.8 K)                                  |
| Wall pressure ratio, $p_{\text{ref}}/p_0$                            | 0.6072 (-0.0016, +0.0016)                               |
| Exit wall pressure ratio, $p_{\text{exit}}/p_0$                      | 0.5825 (-0.0018, +0.0018)                               |
| Reference Mach number, $M_{\text{ref}}$                              | 0.8747 (-0.006, +0.005)                                 |
| Reference Reynolds number, $Re_{c,\text{ref}}$                       | 971,900 (-61,100, +68,000)                              |
| Reference velocity, $u_{\text{ref}}$                                 | 294.1 (-4.8, +3.2 m/s)                                  |
| Empty tunnel wall boundary-layer thickness, $\delta_{99,\text{ref}}$ | 11.9 (-0.3, +0.3 mm)                                    |
| Turbulence intensity   | 0.23% (-0.01, +0.01%)                                   |

boundary layer [34]. Again, the fit was only applied to points above  $y^+ = 70$ . Results are normalized by the boundary-layer edge velocity  $u_e$ . The 99% boundary-layer thickness is 1.8 mm, displacement thickness is 0.4 mm, and momentum thickness is 0.2 mm. Displacement and momentum thicknesses were calculated using a density profile via the Crocco–Busemann relation [35].

The reported conditions in the previous sections are summarized in Table 2. Note that the Reynolds number is defined based on the chord  $c$ , with additional details in the Appendix. These reported conditions are sufficient to prescribe RANS simulation inputs.

### B. Surface Flow Topology

The shock, separation, and reattachment locations correspond to different surface shear stresses, producing distinct patterns in oil-flow visualizations. This was acquired early in the experimental campaign to identify the variation of flow topology with Mach number, and the critical Mach number where the shock and separation locations coalesce. Images were acquired during the steady run time to prevent bias from tunnel start/stop transients. The mean and fluctuating intensity of the images were calculated, and the topology manually identified as shown in Fig. 9. The shock was identified by a discontinuous increase in oil signal, with oil continuing to move downstream. Separation was identified by oil pooling at a saddle point between downstream and upstream flowing oil. Reattachment was identified as a “source” where the oil flow is in opposite directions. For  $M_{\text{ref}} < 0.875$ , the shock and separation locations are separate and distinct, indicating that the shock is not strong enough to cause an immediate separation of the incoming boundary layer. At  $M_{\text{ref}} = 0.875$ , the shock and separation regions nearly coalesce, with the shock located at  $x/c = 0.66$  and the separation at  $x/c = 0.68$ , indicating that the shock is inducing the separation. The reattachment position for  $M_{\text{ref}} = 0.875$  is at  $x/c = 1.23$ . For  $M_{\text{ref}} > 0.875$ , very slight downstream movement of the shock and separation is observed, and the reattachment position moves significantly, to  $x/c = 1.35$  at  $M_{\text{ref}} = 0.895$ . For the remainder of the paper, the case at  $M_{\text{ref}} = 0.875$  is studied as it is the first Mach number exhibiting a shock-induced separation.

### C. Surface Pressure

The surface pressure coefficient along the axis in the vicinity of the bump is given in Fig. 10, and is defined as

$$C_p = \frac{2}{\gamma M_{\text{ref}}^2} \left( \frac{p}{p_{\text{ref}}} - 1 \right)$$

where the reference normalization values are given in Table 2. The relevant topology locations are also plotted, from the estimates provided later in Sec. IV.B. The pressure coefficient is azimuthally averaged from the data shown in Fig. 10c, where the masked areas are not included in the averaging. Upstream of the shock, the flow is axisymmetric. A slight asymmetry is observed at the separation and

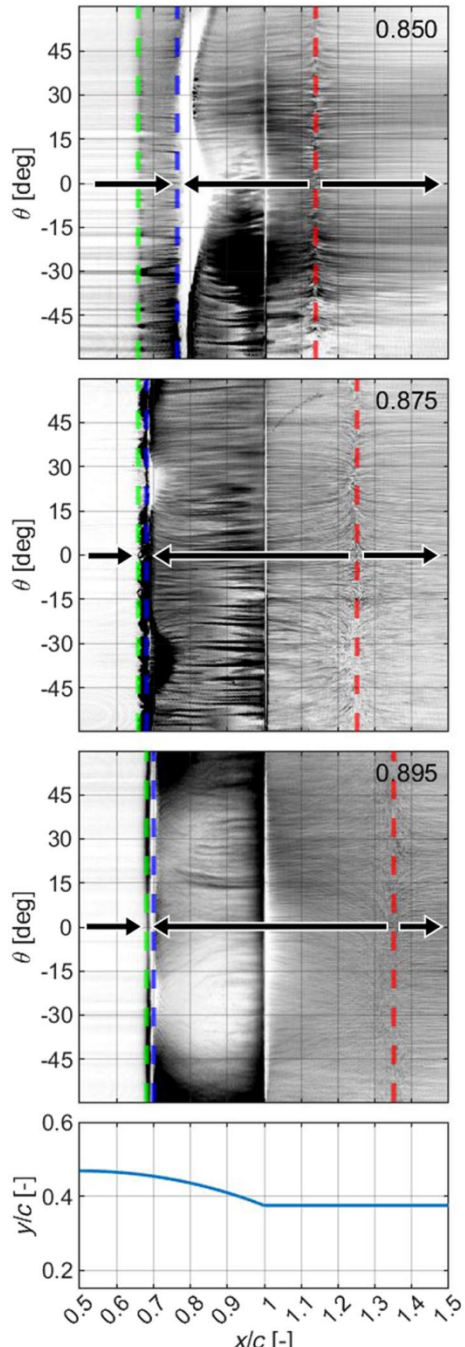


**Fig. 9** Oil-flow visualizations for  $M_{\text{ref}} = 0.85$  (first row),  $0.875$  (second row), and  $0.895$  (third row) with annotated topology locations: green line, shock; blue line, separation; red line, reattachment. Arrows show the direction of flow movement between locations. Fourth row is axis-matched model contour.

reattachment location. Note that  $C_p$  is nonzero upstream of the bump due to the definition of the reference condition on the tunnel wall. An acceleration of the flow occurs before the apex of the bump, causing a reduction in pressure to a minimum value of  $-0.7$  at  $x/c = 0.55$ . Following this, the pressure recovers due to the combined influence of decreasing model area (increasing flow area) and the pressure rise across the shock. Downstream of the separation location, the curvature of the pressure variation changes and plateaus around  $-0.15$  in the recirculation region. Through the reattachment region, the pressure recovers to a positive value.

### D. Surface Shear Stress

The surface skin friction coefficient  $C_f$  is shown in Fig. 11. Due to the limited extent of each OFI interrogation region, the measurement

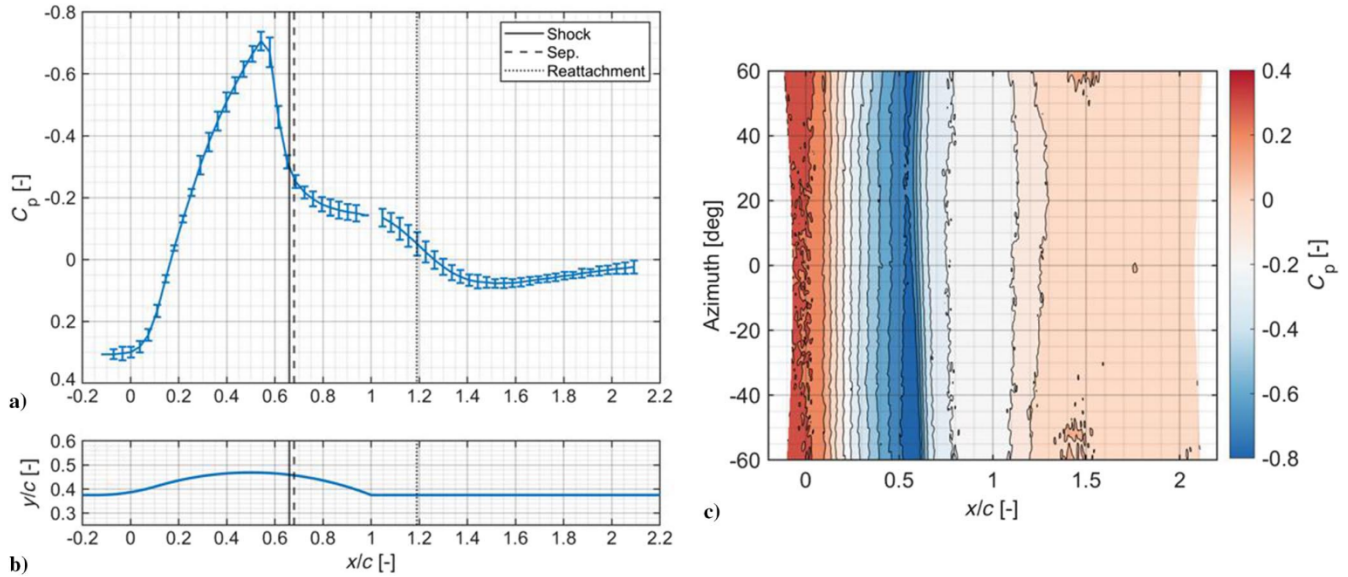


Fig. 10 a) Surface pressure coefficient at  $M_{ref} = 0.875$ . Note the reverse y axis following Bachalo and Johnson [13]. b) Axis-matched model contour. c) Azimuthal distribution of pressure coefficient. Shock, separation, and reattachment locations from combined estimates of Sec. IV.A.

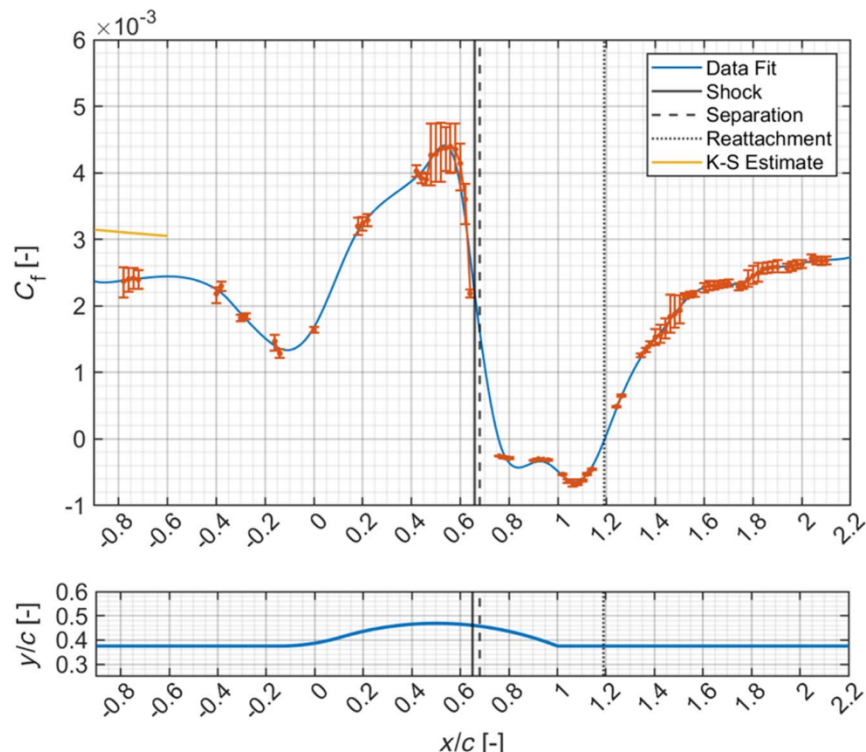


Fig. 11 Top: surface skin friction coefficient at  $M_{ref} = 0.875$ . Experimental data given as red points with uncertainty bands. Fit (blue) is a smoothing spline to illustrate trends between measurement locations. Bottom, axis-matched model contour. Shock, separation, and reattachment locations from combined estimates of Sec. IV.A.

is sparser than the previous pressure measurements. Upstream of the bump,  $C_f$  is approximately 0.0025, consistent with the development of a turbulent boundary layer from the trip location of  $x/c = -2.5$  given by the Karman–Schoenherr relation with a compressibility correction of 0.95 [36]. This value decreases to a minimum of approximately 0.0013 at the beginning of the upstream fillet of the bump. As the flow accelerates over the bump, the skin friction drastically increases to a maximum of 0.0044 at the apex location of  $x/c = 0.5$ . Slightly upstream of the separation location, the skin friction plummets rapidly, crossing zero at approximately  $x/c = 0.69$ , consistent with separation. The skin friction plateaus at a negative value for the remainder of the curved section of the

bump, indicative of reverse flow, and exhibits a second drop at the geometric discontinuity at  $x/c = 1.0$ . A second zero-crossing occurs during the flow reattachment at approximately  $x/c = 1.18$ , caused by the flow direction reversal. Following reattachment, the flow recovers to a skin friction of 0.0027, slightly higher than the incoming flow.

#### E. Velocity

The mean  $u$ - and  $v$ -velocity components of the planar velocity field from PIV are shown in Fig. 12, with associated extracted line plots in Fig. 13. The profiles are at recommended locations for validation comparison and include uncertainty bands. Upon reaching

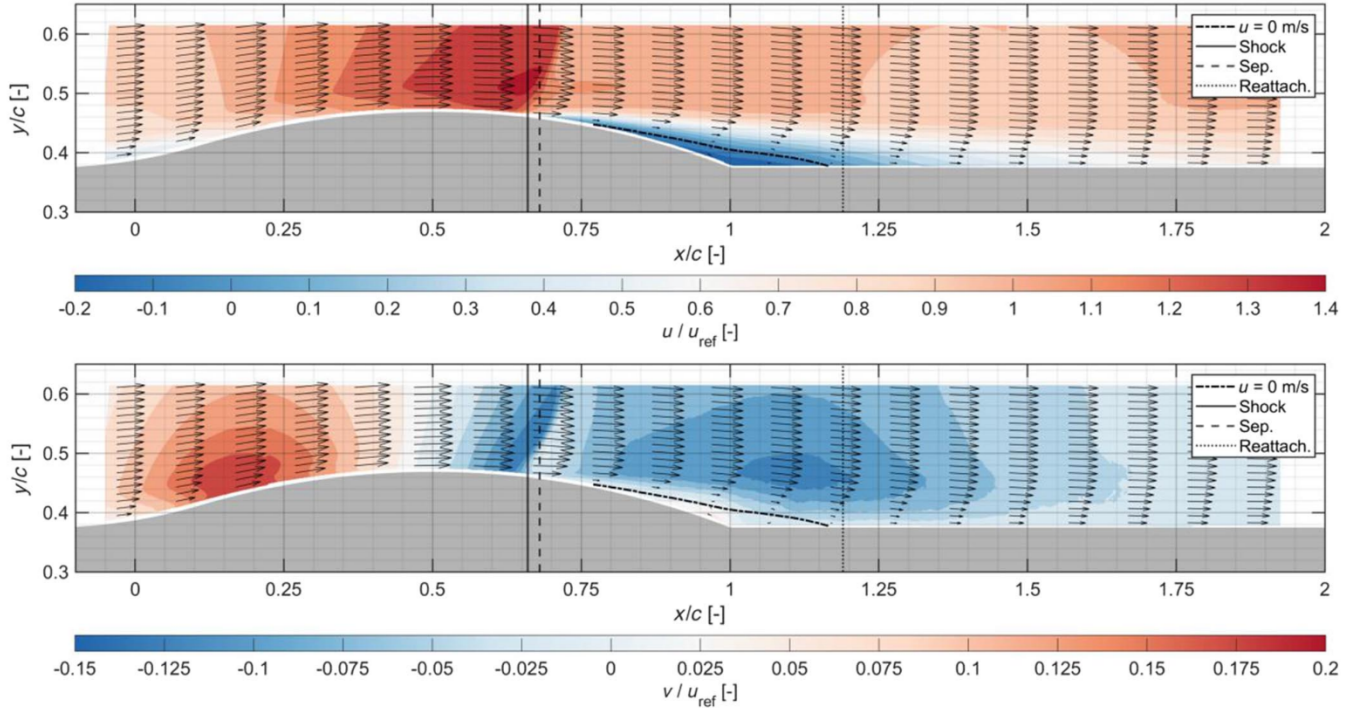


**Fig. 12** Top: mean  $u$ -component of velocity. Bottom: mean  $v$ -component. Line contour represents  $u = 0$  m/s. Velocity normalized by  $u_{\text{ref}}$ , defined in Table 2. Shock, separation, and reattachment locations from combined estimates of Sec. IV.A.

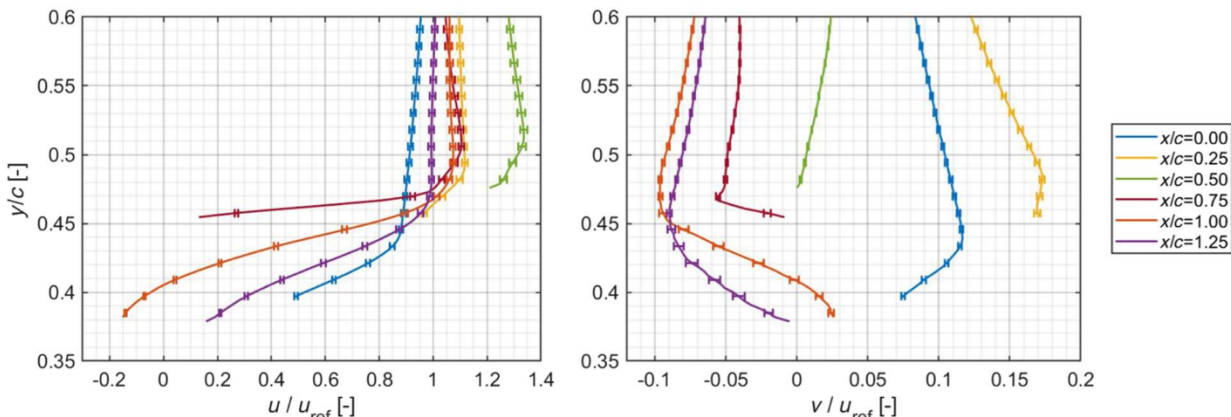


**Fig. 13** Line plots of mean  $u$ -component of velocity (left) and  $v$ -component (right) at profile locations throughout the interaction.

the upstream edge of the hump (at  $x/c = 0$ ) the BL experiences a favorable pressure gradient and accelerates up the forward face. This results in a decrease of the BL thickness up to the apex as shown by the upstream profiles (profiles at  $x/c = 0.25$  and  $0.50$ ). The flow accelerates by over 100 m/s at the apex, reaching a peak velocity of 416 m/s immediately upstream of the shock at approximately  $x/c = 0.65$ . Assuming isentropic compression from the reference velocity, this corresponds to a peak Mach number of approximately 1.34. This is consistent with related experiments on a circular-arc geometry, which showed that a Mach number of 1.32 was the minimum that produced a pressure rise sufficient to cause separation, with the separation point coalescing with the shock for  $M > 1.34$  [37].

After the apex, the flow turns downward (profile at  $x/c = 0.75$ ) and experiences an adverse pressure gradient. The separation is identified at  $x/c = 0.68$  by the most upstream location of reverse flow as indicated by the intersection of the  $u = 0$  m/s contour with the model (dot-dashed line in Fig. 12). The separation bubble grows with further downstream distance with visible flow reversal near the wall (negative  $u$  in the  $x/c = 1.0$  profile in Fig. 13). The bubble reaches a maximum transverse height of about 0.1  $y/c$  above the model at  $x/c = 1.05$ . Slightly downstream of this, the outer flow turns downward toward the model leading to reattachment at

$x/c = 1.17$ . The turbulent boundary layer then begins to recover (profile at  $x/c = 1.25$  in Fig. 13) and continues its recovery for the remainder of the FOV. The favorable pressure gradient and acceleration on the forward face of the bump result in a decrease of the boundary-layer thickness upstream of the shock as shown by upstream profiles in Fig. 13.

The Reynolds normal and shear stresses are shown in Fig. 14, with associated extracted line plots in Fig. 15. Reynolds stresses illustrate the turbulent transport of momentum throughout the shear layer and are connected to mixing-layer growth. Note that the Reynolds stresses are given in the Cartesian frame and are *not* rotated to align with the local streamwise direction. The Reynolds stresses decrease until the shock location of  $x/c = 0.65$ , indicating a stable shock location with minimal jitter of the shock foot. The unsteadiness of the shock, although small, results in a peak stress at the mean shock location, which decreases as the shock interacts with the lower-velocity flow within the boundary layer. The profiles provide a more quantitative perspective on Reynolds stresses with associated uncertainties. They highlight the expected behavior of suppressed stresses on the upstream part of the hump due to the favorable pressure gradient and augmented stresses downstream whose peaks are observed farther from the wall in the separation region.

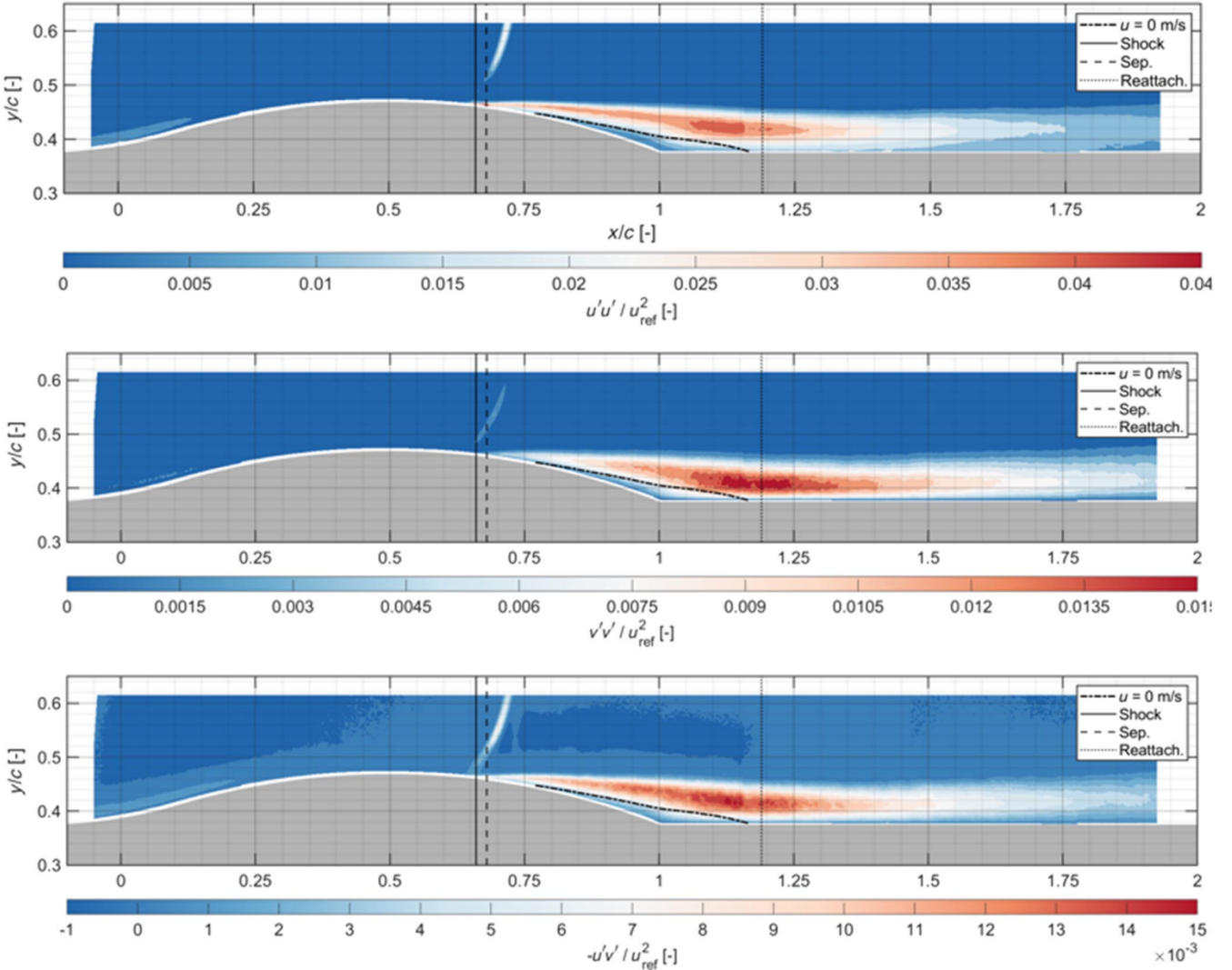


Fig. 14 Contours of Reynolds stresses,  $u'u'$  (top),  $v'v'$  (middle), and  $-u'v'$  (bottom) normalized by  $u_{ref}^2$ . Shock, separation, and reattachment locations from combined estimates of Sec. IV.A. Line contour represents  $u = 0$  m/s.

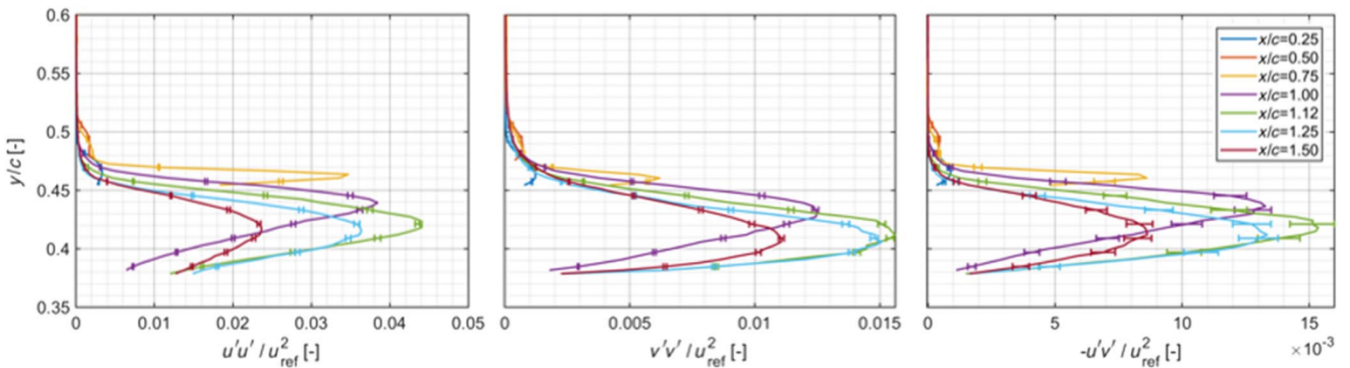
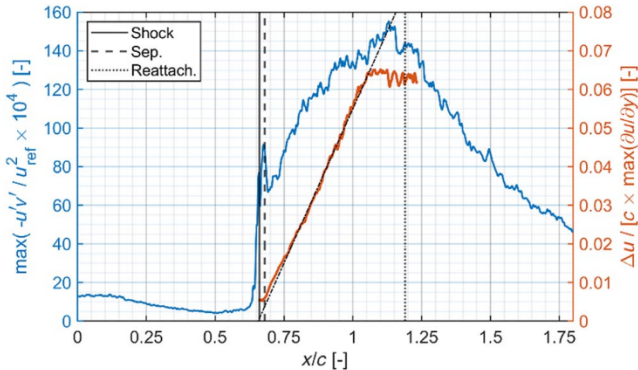


Fig. 15 Line plots of Reynolds stresses,  $u'u'$  (left),  $v'v'$  (middle), and  $-u'v'$  (right) normalized by  $u_{ref}^2$  at profile locations throughout the interaction. Note that uncertainty bands are only shown for a subset of the data for clarity.

The Reynolds shear stress increases sharply after separation and continues to grow as the separated shear layer forms and moves further from the surface. The peak Reynolds stresses occur around  $x/c = 1.125$ , slightly upstream of reattachment. These peak values are consistent with the Reynolds stresses measured in both compressible planar [38] and axisymmetric [39] shear layers.

The maximum shear stress and vorticity thickness at each streamwise location are shown in Fig. 16. The shear layer grows linearly in the region of  $x/c = 0.65$  to 1.05 at a normalized rate of 0.16, which

matches the growth rate for transonic planar shear layers [40]. The Reynolds stress increase correlates with the increasing size of the shear layer, until the shear layer growth is constrained by interaction with the wall. The region from  $x/c = 1.05$  through reattachment is characterized by a constant vorticity thickness as previously reported [40]. Following this, reattachment occurs, which reduces the magnitude of the shear and begins the recovery process for the turbulent boundary layer. The full recovery was not visible within the field of view of the measurement.



**Fig. 16** Streamwise distribution of the maximum Reynolds shear stress and vorticity thickness. Dot-dashed diagonal line is a fit to the linear growth region of vorticity thickness.

#### IV. Discussion

##### A. Positions of Flow Features

The determination of the locations of shock, separation, and reattachment was possible using multiple diagnostic techniques. From the oil-flow visualization, all positions were directly estimated by inspection of calibrated images. For OFI, the shock was identified by observing a marked change in fringe spacing upstream of separation, which was identified by the pooling of oil. OFI is unable to determine an exact position of reattachment; however, the  $C_f$  zero-crossing was estimated based on linear interpolation. Using PIV, the shock location was estimated by the extrapolation of the peak Reynolds stress associated with the shock to the model surface. The PIV separation and reattachment positions were estimated by the intersection of the  $u = 0$  m/s contour with the model surface. These independent methods were combined to estimate the mean value and uncertainty in Table 3.

##### B. Possible Relaminarization

The Reynolds number based on chord of the present experiment (approximately 1 million) is lower than the B-J experiment (2.7 million). This choice was intentional to aid simulations using scale-resolving approaches. However, the lower Reynolds number increased

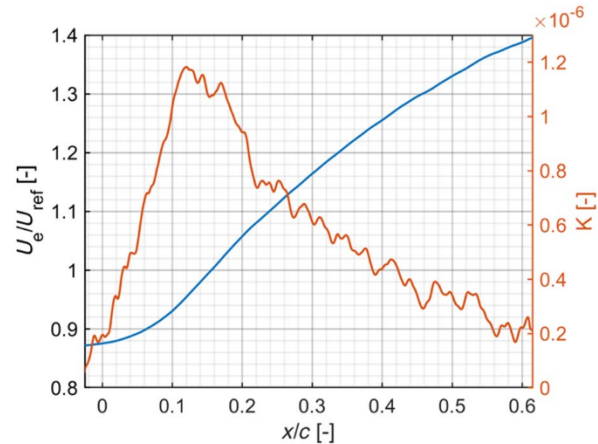


**Fig. 18** Boundary-layer edge velocity and Launder pressure gradient parameter.

the possibility of relaminarization occurring before the shock and separation due to the accelerating flow and the presence of a favorable pressure gradient. In Fig. 17, a contour plot depicts the Reynolds normal stress distribution within the incoming boundary layer. As the flow negotiates the bump, the normal stress reduces by approximately 80% from its incoming value. However, this is still far above the freestream value of approximately  $3 \text{ m}^2/\text{s}^2$ , indicating that the boundary layer is still turbulent.

An approach to quantitatively identify relaminarization is to use Launder's pressure gradient parameter defined as

$$K = \frac{\nu \frac{\partial U_e}{\partial x}}{U_e^2} \quad (1)$$

where a value of  $3 \times 10^{-6}$  is considered a threshold below which reversion to laminar flow will "eventually ensue" [41]. The peak value found in this work was approximately  $K \approx 1.2 \times 10^{-6}$ , as depicted in Fig. 18, and is thus well below Launder's threshold. These two analyses suggest that the flow remains turbulent throughout the acceleration, but with reduced turbulent stresses going into the shock interaction compared to a canonical turbulent boundary layer.

##### C. Axisymmetry

This experiment tested an axisymmetric geometry in a square, solid-wall tunnel. It was anticipated that minor deviations from axisymmetry could be impressed on the flow by this configuration. The experiments most sensitive to these effects are the oil-flow visualization and PSP. For the oil-flow, some evidence of faint lobes can be seen in Fig. 9. This indicates a bulk three-dimensionality

**Table 3** Flow feature positions

| Measurement | Shock           | Separation      | Reattachment          |
|-------------|-----------------|-----------------|-----------------------|
| Oil-flow    | 0.66            | 0.68            | 1.23                  |
| OFI         | 0.66            | 0.69            | 1.18                  |
| PIV         | 0.65            | 0.68            | 1.17                  |
| Combined    | $0.66 \pm 0.01$ | $0.68 \pm 0.01$ | $1.19 (-0.02, +0.04)$ |

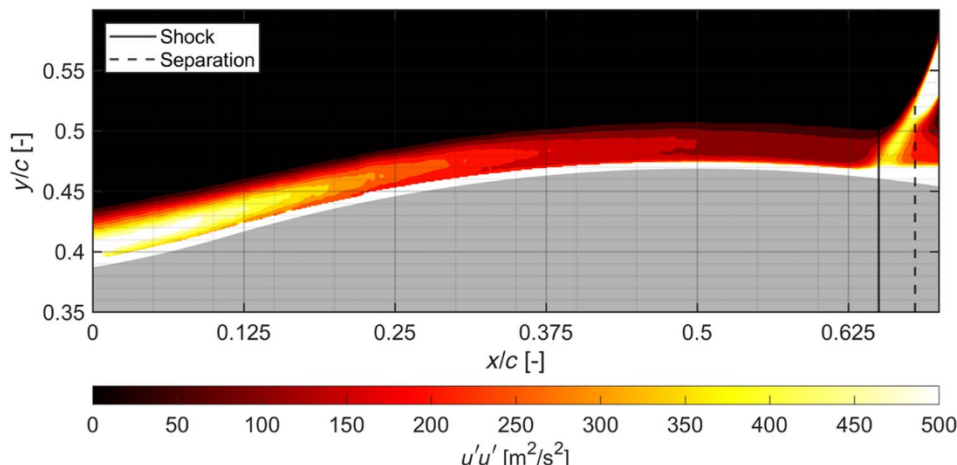


**Fig. 17** Reynolds normal stress upstream of the shock and separation locations.

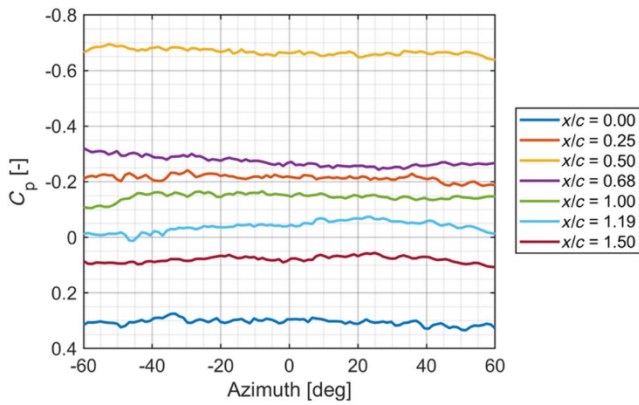


**Fig. 19** Azimuthal variation in pressure coefficient at multiple axial locations.

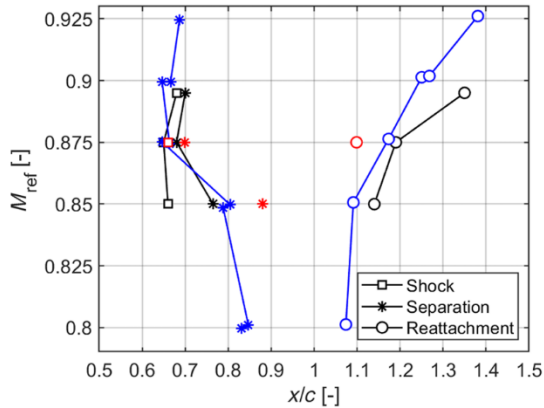


**Fig. 20** Topology locations with varying Mach number. Black symbols are data from this experiment ( $M_{\text{ref}} = 0.85$  and  $0.895$  acquired in separate runs). Bachalo–Johnson configuration shown in red points from [13] with additional data points in blue from Johnson et al. [12].

within the recirculation region; however, the location of the shock, separation, and reattachment shows no signs of variation across the azimuth. For the PSP, a slight azimuthal variation in the pressure at the shock location can be seen in Fig. 10, but within a small fraction of a chord length. This is further clarified in Fig. 19, which shows the pressure coefficient as a function of the azimuth throughout the interaction. Some asymmetry is present between  $x/c = 0.68$  to 1.5, but there is no evidence of 90 deg periodicity that would be expected for a square test section. Thus, the available data show the flow to be approximately axisymmetric.

#### D. Comparison to Bachalo–Johnson

This experiment was inspired by, but is not a direct replica of, the B-J test [13]. The geometry is scaled, and there are subtle differences

in the blending of the forebody and the bump. The elliptical nose shape and trip are different, and the Reynolds number is lower. However, a similar Mach number was maintained. Therefore, a comparison of the experimental data is warranted to highlight resulting differences, without an expectation that the results should match. In Fig. 20, comparisons are shown of the topology variation with Mach number as identified through oil-flow visualization. Additional data on the B-J configuration at different Mach numbers are provided by Johnson et al. [12]. For  $M_{\text{ref}} < 0.875$ , both experiments show the shock and separation locations as distinct, and these coalesce at and above  $M_{\text{ref}} = 0.875$ . After coalescing, the shock/separation location is insensitive to Mach number. The reattachment location differs between the experiments but exhibits the same trend in moving downstream as Mach number increases.

In Fig. 21, the velocity and Reynolds shear stress profiles are compared. Good agreement of velocity is obtained for the incoming boundary-layer profiles and early portions of the separated region. For  $x/c > 1$ , deviations are more apparent near the wall, indicating a change in the momentum transfer in the later part of the separation region and reattachment.

Notable differences are observed in the Reynolds shear stress: in the present experiment the incoming boundary layer at  $x/c = 0.69, y/c \approx 0.48$  has approximately half the shear stress of the B-J experiment. This is consistent with the earlier discussion on relaminarization and the lower Reynolds number of the present experiment. This appears to have a consequence throughout the interaction, where at every station from  $0.81 < x/c < 1.25$  the peak Reynolds shear stress is lower than in the B-J experiment. The maximum shear stress at  $x/c = 1.12$  is approximately 25% lower than the B-J experiment. The significant peak in the Reynolds stress at  $x/c = 0.69$  is caused by the shock passing through this measurement location. In the B-J experiment, the shock was located further downstream and does not influence the  $x/c = 0.69$  location.

A comparison of the pressure distribution is shown in Fig. 22. There are significant differences in the pressure between the two

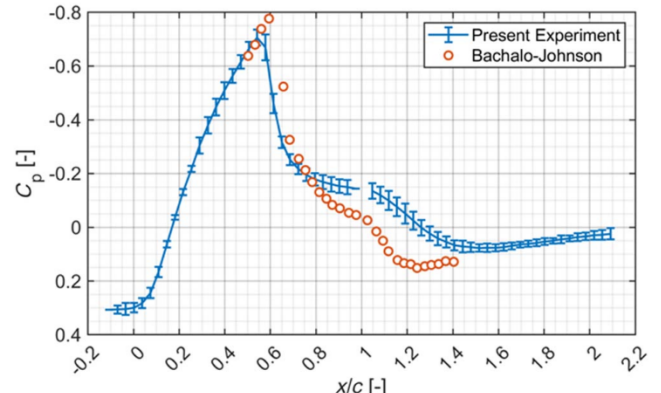


**Fig. 22** Comparison of the pressure coefficient. Lines with uncertainty bands are present experiment; points are from [13] as digitized in [15].

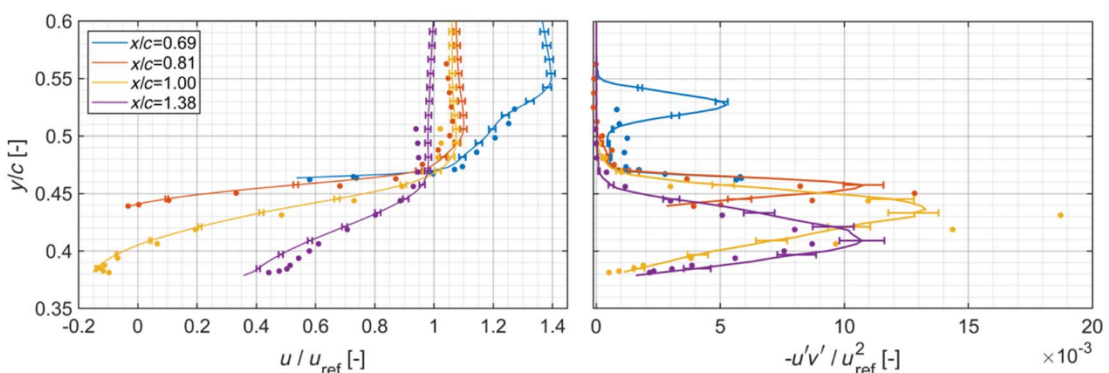


**Fig. 21** Comparison of  $u$ -velocity (left) and normalized Reynolds shear stress  $-u'v'$  (right). Lines with uncertainty bands are present experiment; points are from [13] as digitized in [15].

experiments: first, the location of the shock is slightly further upstream in the present experiment, possibly due to the influence of the solid sidewall or lower turbulence level in the incoming boundary layer. Second, the separated region is longer in the present experiment, consistent with the reattachment locations shown in Fig. 20.

## V. Conclusions

An experimental characterization of transonic, turbulent, separated flow generated by an axisymmetric model was presented that is of sufficient quality and completeness to be used as a validation data source. The geometry was inspired by the B-J experiment and consisted of a circular bump on a constant-diameter cylinder operated at a reference Mach number of 0.875 and Reynolds number of approximately 1 million. A characterization of the wind tunnel flow conditions was provided to support computational comparisons to the experiment. PIV, PSP, oil-flow visualization, and oil-film interferometry were applied to measure properties of the incoming boundary layer, the shock/separation interaction region, the detached shear layer and reverse flow region, and reattachment. Each measurement was reported with a quantified uncertainty from random and bias sources. These measurements were combined to provide estimates of the shock, separation, and reattachment locations. Surface shear stress, mean surface pressure, mean velocity fields, and Reynolds stress distributions throughout the flow were provided. Despite a reduction in incoming turbulent shear stress in the accelerating flow over the bump, the flow did not relaminarize, and the peak-normalized Reynolds shear stress in the detached shear layer was  $1.5 \times 10^{-2}$ . This variation in incoming shear stress and high shear stress following separation may be a challenge for current RANS turbulence models. The measurements of velocity, surface shear stress, surface pressure, and flow topology provide a rich data set for turbulence model development and validation studies. The dataset has been made available on the Turbulence Modeling Resource website for public use [15].

## Appendix: Uncertainty Propagation

Uncertainty propagation was conducted following recommendations of Coleman and Steele [42], where systematic/bias and random uncertainties sources were combined such as  $U_i = \sqrt{B_i^2 + S_i^2}$ , where  $U_i$  is the expanded total uncertainty for quantity  $i$ ,  $B_i$  is the expanded bias uncertainty from sensors and data acquisition hardware, and  $S_i$  is the random uncertainty. This random uncertainty is generally quantified by the range that captures 95% of the data and accounts for condition variability during and between tests, turbulent quantities that are inherently unsteady, and sensor noise.

This  $U_i$  equation is used directly for measured quantities of interest such as stagnation temperature and pressure. However, many quantities of interest in this work shown in Table 2 are the result of a data reduction equation where measured quantities are combined into a derived quantity. One example is the Mach number from the isentropic relation:

$$M = \sqrt{\left[\left(\frac{p_0}{p}\right)^{(y-1)/y} - 1\right]\left(\frac{2}{y-1}\right)}$$

---


$$U_M = \sqrt{\left(\frac{\gamma p \left(\frac{p_0}{p}\right)^{1/y} - p_0 \left(\frac{p_0}{p}\right)^{(1-y)/y}}{\gamma R T_0 p \left(\frac{p_0}{p}\right)^{2/y}}\right)^2 U_{p_0}^2 + \left(\frac{p_0}{R T_0^2 \left(\frac{p_0}{p}\right)^{1/y}}\right)^2 U_{T_0}^2 + \left(\frac{\left(\frac{p_0}{p}\right)^{(y-1)/y}}{\gamma R T_0}\right)^2 U_p^2}$$


---

where  $p_0$  is stagnation pressure,  $p$  is any arbitrary static pressure, and  $y$  is the ratio of specific heats. The uncertainty propagation in such cases is performed with the Taylor series method (TSM) by Coleman and Steele [42] and considers the uncertainty of  $p_0$  and  $p$ , whereas  $y$  is said to be 1.4 for air with negligible uncertainty. The general form of the TSM method applied to Mach number is therefore

$$U_M = \sqrt{\left(\frac{\partial M}{\partial y}\right)^2 U_y^2 + \left(\frac{\partial M}{\partial p_0}\right)^2 U_{p_0}^2 + \left(\frac{\partial M}{\partial p}\right)^2 U_p^2}$$

where  $U_i$  is the expanded uncertainty of parameter  $i$  and uncertainty sources are assumed independent. Here, expanded uncertainty means that a confidence factor coefficient has been applied to the standard uncertainty. In this work, the commonly used factor in engineering is assumed to be 95% such as  $U_i = 2u_i$ . The partial derivatives act as sensitivities between the parameter uncertainties and the uncertainty of the quantity of interest. Since  $U_y \approx 0$ , we will skip solving the partial derivative  $\partial M / \partial y$ . The remaining partial derivatives are solved as

$$\frac{\partial M}{\partial p_0} = \frac{1}{\gamma p \left(\frac{p_0}{p}\right)^{1/y} \sqrt{\left[\left(\frac{p_0}{p}\right)^{(y-1)/y} - 1\right]\left(\frac{2}{y-1}\right)}}$$

$$\frac{\partial M}{\partial p} = -\frac{p_0}{\gamma p^2 \left(\frac{p_0}{p}\right)^{1/y} \sqrt{\left[\left(\frac{p_0}{p}\right)^{(y-1)/y} - 1\right]\left(\frac{2}{y-1}\right)}}$$

The simplified Mach number uncertainty general equation is therefore

$$U_M = \sqrt{\frac{p^2 U_{p_0}^2 + p_0^2 U_p^2}{\gamma^2 p^4 \left(\frac{p_0}{p}\right)^{2/y} \left[\left(\frac{p_0}{p}\right)^{(y-1)/y} - 1\right]\left(\frac{2}{y-1}\right)}}$$

Following these same methods, the uncertainty in the pressure ratio for arbitrary  $p_i$  normalized by  $p_0$  is therefore

$$U_{p_i/p_0} = \sqrt{\left(\frac{U_{p_i}}{p_0}\right)^2 + \left(\frac{p_i U_{p_0}}{p_0^2}\right)^2}$$

The Reynolds number was calculated by  $Re = (\rho u L / \mu)$  where  $\rho$  is fluid density,  $u$  is bulk velocity,  $L$  is the characteristic length taken as the chord length, and  $\mu$  is fluid dynamic viscosity. The partial derivatives are straightforward, and the resulting uncertainty is

$$U_{Re} = L \sqrt{\left(\frac{u U_\rho}{\mu}\right)^2 + \left(\frac{\rho U_u}{\mu}\right)^2 + \left(\frac{\rho u U_\mu}{\mu^2}\right)^2}$$

where  $U_\rho$  is the uncertainty of  $\rho$ ,  $U_u$  is the uncertainty of  $u$ , and  $U_\mu$  is the uncertainty of  $\mu$ . Here uncertainty in  $L$  is expected to be negligible. There are three new uncertainty sources that need to be defined.

The fluid density was calculated by

$$\rho = \frac{\rho_0}{\left(1 + \frac{y-1}{2} M^2\right)^{1/(y-1)}}$$

and stagnation density as  $\rho_0 = (p_0 / RT_0)$ , where  $R$  is the gas constant and  $T_0$  is the stagnation temperature. Substituting  $\rho_0$  and  $M$  definitions into the equation for  $\rho$  and performing the TSM with partial derivatives, the resulting uncertainty for density is

$$U_\rho = \sqrt{\left(\frac{\gamma p \left(\frac{p_0}{p}\right)^{1/y} - p_0 \left(\frac{p_0}{p}\right)^{(1-y)/y}}{\gamma R T_0 p \left(\frac{p_0}{p}\right)^{2/y}}\right)^2 U_{p_0}^2 + \left(\frac{p_0}{R T_0^2 \left(\frac{p_0}{p}\right)^{1/y}}\right)^2 U_{T_0}^2 + \left(\frac{\left(\frac{p_0}{p}\right)^{(y-1)/y}}{\gamma R T_0}\right)^2 U_p^2}$$

where  $U_{p_0}$  is the stagnation pressure uncertainty,  $U_{T_0}$  is the stagnation temperature uncertainty, and  $U_p$  is the static pressure uncertainty.

The velocity was calculated from  $u = M \sqrt{\gamma RT}$ . Since the stagnation temperature was measured, the relation

$$T = \frac{T_0}{1 + \frac{y-1}{2} M^2}$$

was used to provide the static temperature. Substituting  $T$  into the  $u$  equation and doing TSM, the velocity uncertainty is

$$U_u = \sqrt{\left(\frac{U_{T_0}}{1 + \frac{\gamma-1}{2}M^2}\right)^2 + \left(\frac{T_0M(1-\gamma)U_M}{\left(1 + \frac{\gamma-1}{2}M^2\right)^2}\right)^2}$$

An alternative form of Sutherland's law was used for fluid dynamic viscosity to simplify the partial derivatives as in  $\mu = (C_1 T^{3/2})/(T + S)$ , where  $C_1 = 1.458 \times 10^{-6} \text{ kg}/(\text{m s } \sqrt{\text{K}})$  and  $S = 111 \text{ K}$  for air. Like before but with only one uncertain parameter, the uncertainty of  $\mu$  is therefore

$$U_\mu = C_1 \left( \frac{\frac{3}{2} \sqrt{T}(T + S) - T^{3/2}}{(T + S)^2} \right) U_T$$

Following the uncertainty process for  $T$ ,

$$U_T = \sqrt{\left(\frac{U_{T_0}}{1 + \frac{\gamma-1}{2}M^2}\right)^2 + \left(\frac{T_0M(1-\gamma)U_M}{\left(1 + \frac{\gamma-1}{2}M^2\right)^2}\right)^2}$$

The pressure coefficient is defined as

$$C_p = \frac{2}{\gamma M_{\text{ref}}^2} \left( \frac{p}{p_{\text{ref}}} - 1 \right)$$

The uncertainty in  $C_p$  can be estimated from a Taylor series expansion to yield

$$U_{C_p} = 2 \sqrt{\frac{2(p_{\text{ref}} - p)^2 U_{M_{\text{ref}}}^2}{\gamma^2 M_{\text{ref}}^6 p_{\text{ref}}^2} + \frac{U_p^2}{\gamma^2 M_{\text{ref}}^4 p_{\text{ref}}^2} + \frac{p^2 U_{p_{\text{ref}}}^2}{\gamma^2 M_{\text{ref}}^4 p_{\text{ref}}^4}}$$

The uncertainties in Mach number and reference conditions are specified by transducer data propagation. The pressure is measured using PSP; thus its uncertainty is evaluated from a Taylor series as

$$U_p = \sqrt{\left\{ p_a \left[ 2c_1 \left( \frac{I_0}{I} \right) + c_2 \right] \right\}^2 U_{\frac{I_0}{I}}^2 + \left[ p_a \left( \frac{I_0}{I} \right)^2 \right]^2 U_{c_1}^2 + \left[ p_a \left( \frac{I_0}{I} \right) \right]^2 U_{c_2}^2 + p_a^2 U_{c_3}^2 + \left[ c_1 \left( \frac{I_0}{I} \right)^2 + c_2 \left( \frac{I_0}{I} \right) + c_3 \right]^2 U_{p_a}^2}$$

where  $p_a$  is the ambient pressure during wind-off imaging,  $c_i$  are the calibration coefficients for the polynomial fit, and  $U_{c_i}$  are their associated 95% confidence intervals. The remaining uncertainty is the intensity ratio

$$U_{\frac{I_0}{I}} = \sqrt{\left[ \frac{G_i}{G_0 R_i} \right]^2 U_{R_0}^2 + \left[ \frac{R_0 G_i}{R_i^2 G_0} \right]^2 U_{R_i}^2 + \left[ \frac{R_0 G_i}{R_i G_0^2} \right]^2 U_{G_0}^2 + \left[ \frac{R_0}{R_i G_0} \right]^2 U_{G_i}^2}$$

where the uncertainties are defined on a pixel-by-pixel basis by the standard deviation of intensity over time for both wind-off and wind-on conditions.

### Acknowledgments

The authors thank Russell Spillers, Seth Spitzer, Charley Downing, Marie de Zetter, and Raj Bhakta for their support with wind tunnel operations. The authors also thank Jonathan Naughton for his assistance with oil-film interferometry. Jonathan Naughton, Bart Smith, Chris Roy, and Lian Duan are also acknowledged for their

advisory role throughout the project. Sandia National Laboratories is a multimission laboratory managed and operated by National Technology & Engineering Solutions of Sandia, LLC, a wholly owned subsidiary of Honeywell International, Inc., for the U.S. Department of Energy's National Nuclear Security Administration under contract DE-NA0003525. This paper describes objective technical results and analysis. Any subjective views or opinions that might be expressed in the paper do not necessarily represent the views of the U.S. Department of Energy or the United States Government.

### References

- [1] Lee, B. H. K., "Self-Sustained Shock Oscillations on Airfoils at Transonic Speeds," *Progress in Aerospace Sciences*, Vol. 37, No. 2, 2001, pp. 147–196.  
[https://doi.org/10.1016/S0376-0421\(01\)00003-3](https://doi.org/10.1016/S0376-0421(01)00003-3)
- [2] Babinsky, H., and Harvey, J. K., *Shock Wave-Boundary Layer Interactions*, Cambridge Univ. Press, Cambridge, MA, 2011, Chap. 3.
- [3] Deck, S., "Recent Improvements in the Zonal Detached Eddy Simulation (ZDES) Formulation," *Theoretical and Computational Fluid Dynamics*, Vol. 26, Oct. 2012, pp. 523–550.  
<https://doi.org/10.1007/s00162-011-0240-z>
- [4] Rumsey, C. L., Gatski, T. B., Sellers, W. L., III, Vatsa, V. N., and Viken, S. A., "Summary of the 2004 Computational Fluid Dynamics Validation Workshop on Synthetic Jets," *AIAA Journal*, Vol. 44, No. 2, 2006, pp. 194–207.  
<https://doi.org/10.2514/1.12957>
- [5] Greenblatt, D., Paschal, K. B., Yao, C.-S., Harris, J., Schaeffler, N. W., and Washburn, A. E., "Experimental Investigation of Separation Control Part 1: Baseline and Steady Suction," *AIAA Journal*, Vol. 44, No. 12, 2006, pp. 2820–2830.  
<https://doi.org/10.2514/1.13817>
- [6] Simmons, D. J., "An Experimental Investigation of Smooth-Body Flow Separation," Doctoral Dissertation, Univ. of Notre Dame, Notre Dame, IN, 2020.  
<https://doi.org/10.7274/zs25x63732m>
- [7] Song, S., and Eaton, J. K., "Reynolds Number Effects on a Turbulent Boundary Layer with Separation, Reattachment, and Recovery," *Experiments in Fluids*, Vol. 36, Nov. 2004, pp. 246–258.  
<https://doi.org/10.1007/s00348-003-0696-8>
- [8] Gray, P., Gluzman, I., Thomas, F., Corke, T., Lakebrink, M. T., and Mejia, K., "A New Validation Experiment for Smooth-Body Separation," *AIAA Aviation*, AIAA Paper 2021-2810, 2021.  
<https://doi.org/10.2514/6.2021-2810>
- [9] Bell, J. H., Heineck, J. T., Zilliac, G., Mehta, R. D., and Long, K. R., "Surface and Flow Field Measurements on the FAITH Hill Model," *AIAA Aerospace Sciences Meeting*, AIAA Paper 2012-704, 2012.  
<https://doi.org/10.2514/6.2012-704>
- [10] Gargiulo, A., Duetsch-Patel, J. E., Ozoroski, T. A., Beardsley, C., Vishwanathan, V., Fritsch, D., Borgoltz, A., Devenport, W. J., Roy, C. J., and Lowe, K. T., "Flow Field Features of the BEVERLI Hill Model," *AIAA SciTech*, AIAA Paper 2021-1741, 2021.  
<https://doi.org/10.2514/6.2021-1741>
- [11] Tinoco, E. N., Brodersen, O. P., Keye, S., Laflin, K. R., Feltrop, E., Vassberg, J. C., Mani, M., Rider, B., Wahls, R. A., Morrison, J. H., Hue, D., Roy, C. J., Mavriplis, D. J., and Murayama, M., "Summary Data from the Sixth AIAA CFD Drag Prediction Workshop: CRM Cases," *Journal of Aircraft*, Vol. 55, No. 4, 2018, pp. 1352–1379.  
<https://doi.org/10.2514/1.C034409>
- [12] Johnson, D. A., Horstman, C. C., and Bachalo, W. D., "Comparison Between Experiment and Prediction for a Transonic Turbulent Separated Flow," *AIAA Journal*, Vol. 20, No. 6, 1982, pp. 737–744.  
<https://doi.org/10.2514/3.51130>
- [13] Bachalo, W. D., and Johnson, D. A., "Transonic, Turbulent Boundary-Layer Separation Generated on an Axisymmetric Flow Model," *AIAA Journal*, Vol. 24, No. 3, 1986, pp. 437–442.  
<https://doi.org/10.2514/3.9286>

- [14] Oberkampf, W. L., and Smith, B. L., "Assessment Criteria for Computational Fluid Dynamics Model Validation Experiments," *Journal of Verification, Validation and Uncertainty Quantification*, Vol. 2, No. 3, 2017, Paper 031002. <https://doi.org/10.1115/1.4037887>
- [15] Rumsey, C., "Turbulence Modeling Resource," <https://turbmodels.larc.nasa.gov/> [retrieved 9 May 2022].
- [16] Bradshaw, P., Launder, B. E., and Lumley, J. L., "Collaborative Testing of Turbulence Models," *Journal of Fluids Engineering*, Vol. 118, No. 2, 1996, pp. 243–247. <https://doi.org/10.1115/1.2817369>
- [17] Wilcox, D. C., *Turbulence Modeling for CFD*, DCW Industries, La Canada, CA, 1998, pp. 283–284.
- [18] Spalart, P. R., Belyaev, K. V., Garbaruk, A. V., Shur, M. L., Strelets, M. K., and Travin, A. K., "Large-Eddy and Direct Numerical Simulations of the Bachalo-Johnson Flow with Shock-Induced Separation," *Flow, Turbulence and Combustion*, Vol. 99, No. 3, 2017, pp. 865–885. <https://doi.org/10.1007/s10494-017-9832-z>
- [19] Uzun, A., and Malik, M. R., "Wall-Resolved Large-Eddy Simulations of Transonic Shock-Induced Flow Separation," *AIAA Journal*, Vol. 57, No. 5, 2019, pp. 1955–1972. <https://doi.org/10.2514/1.J057850>
- [20] Aeschliman, D. P., and Oberkampf, W. L., "Experimental Methodology for Computational Fluid Dynamics Code Validation," *AIAA Journal*, Vol. 36, No. 5, 1998, pp. 733–741. <https://doi.org/10.2514/2.461x>
- [21] Oberkampf, W. L., and Trucano, T. G., "Verification and Validation in Computational Fluid Dynamics," *Progress in Aerospace Sciences*, Vol. 38, No. 3, 2002, pp. 209–272. [https://doi.org/10.1016/S0376-0421\(02\)00005-2](https://doi.org/10.1016/S0376-0421(02)00005-2)
- [22] Beresh, S. J., Henfling, J. F., Spillers, R. W., and Erven, R. J., "Measurement of Experimental Boundary Conditions for CFD Validation of a Supersonic Jet in Transonic Crossflow," *AIAA Paper 2006-3449*, 2006. <https://doi.org/10.2514/6.2006-3449>
- [23] Wieneke, B., "PIV Uncertainty Quantification from Correlation Statistics," *Measurement Science and Technology*, Vol. 26, June 2015, Paper 074002. <https://doi.org/10.1088/0957-0233/26/7/074002>
- [24] Baldwin, A., Mears, L. J., Arora, N., Kumar, R., Alvi, F. S., and Naughton, J. W., "Skin Friction Measurements Using Oil Film Interferometry in a 3-D Supersonic Flowfield," *AIAA Journal*, Vol. 57, No. 4, 2019, pp. 1373–1382. <https://doi.org/10.2514/1.J057388>
- [25] Driver, D. M., "Application of Oil-Film Interferometry Skin-Friction Measurement to Large Wind Tunnels," *Experiments in Fluids*, Vol. 34, No. 6, 2003, pp. 717–725. <https://doi.org/10.1007/s00348-003-0613-1>
- [26] Naughton, J. W., Viken, S., and Greenblatt, D., "Skin-Friction Measurements on the NASA Hump Model," *AIAA Journal*, Vol. 44, No. 6, 2006, pp. 1255–1265. <https://doi.org/10.2514/1.14192>
- [27] Naughton, J. W., and Sheplak, M., "Modern Developments in Shear-Stress Measurement," *Progress in Aerospace Sciences*, Vol. 38, Nos. 6–7, 2002, pp. 515–570. [https://doi.org/10.1016/S0376-0421\(02\)00031-3](https://doi.org/10.1016/S0376-0421(02)00031-3)
- [28] Brown, J. L., and Naughton, J. W., "The Thin Oil Film Equation," *NASA TM 1999-208767*, 1999.
- [29] Naughton, J. W., and Liu, T., "Photogrammetry in Oil-Film Interferometry," *AIAA Journal*, Vol. 45, No. 7, 2007, pp. 1620–1629. <https://doi.org/10.2514/1.24634>
- [30] Naughton, J. W., and Hind, M. D., "Multi-Image Oil-Film Interferometry Skin Friction Measurements," *Measurement Science and Technology*, Vol. 24, No. 12, 2013, Paper 124003. <https://doi.org/10.1088/0957-0233/24/12/124003>
- [31] Quinn, M. K., "Binary Pressure-Sensitive Paint Measurements Using Miniaturised, Colour, Machine Vision Cameras," *Measurement Science and Technology*, Vol. 29, No. 5, 2018, Paper 055107. <https://doi.org/10.1088/1361-6501/aaae60>
- [32] Lynch, K., Miller, N., Barone, M., Beresh, S., Spillers, R., Henfling, J., and Soehnel, M., "Revisiting Bachalo-Johnson: The Sandia Axisymmetric Transonic Hump and CFD Challenge," *AIAA Paper 2019-2848*, 2019. <https://doi.org/10.2514/6.2019-2848>
- [33] Scharnowski, S., Bross, M., and Kahler, C. J., "Accurate Turbulence Level Estimations Using PIV/PTV," *Experiments in Fluids*, Vol. 60, No. 1, Nov. 2019. <https://doi.org/10.1007/s00348-018-2646-5>
- [34] Sun, C.-C., and Childs, M. E., "A Modified Wall Wave Velocity Profile for Turbulent Compressible Boundary Layers," *Journal of Aircraft*, Vol. 10, No. 6, 1973, pp. 381–383. <https://doi.org/10.2514/3.44376>
- [35] White, F. M., *Viscous Fluid Flow*, 3rd ed., McGraw-Hill, New York, 2006, Chap. 7.
- [36] Rumsey, C., "Compressibility Considerations for k-omega Turbulence Models in Hypersonic Boundary-Layer Applications," *Journal of Spacecraft and Rockets*, Vol. 47, No. 1, 2010, pp. 11–20. <https://doi.org/10.2514/1.45350>
- [37] Alber, I. E., Bacon, J. W., Masson, B. S., and Collins, D. J., "An Experimental Investigation of Turbulent Transonic Viscous-Inviscid Interactions," *AIAA Journal*, Vol. 11, No. 5, 1973, pp. 620–627. <https://doi.org/10.2514/3.50501>
- [38] Goebel, S. G., and Dutton, J. C., "Experimental Study of Compressible Turbulent Mixing Layers," *AIAA Journal*, Vol. 29, No. 4, 1990, pp. 538–546. <https://doi.org/10.2514/3.10617>
- [39] Freund, J. B., Lele, S. K., and Moin, P., "Compressibility Effects in a Turbulent Mixing Layer. Part 1. Turbulence and Growth Rate," *Journal of Fluid Mechanics*, Vol. 421, Nov. 2000, pp. 229–267. <https://doi.org/10.1017/S0022112000001622>
- [40] Scharnowski, S., Bolgar, I., and Kahler, C. J., "Characterization of Turbulent Structures in a Transonic Backward-Facing Step Flow," *Flow, Turbulence and Combustion*, Vol. 98, 2017, pp. 947–967. <https://doi.org/10.1007/s10494-016-9792-8>
- [41] Jones, W. P., and Launder, B. E., "The Prediction of Laminarization with a Two-Equation Model of Turbulence," *International Journal of Heat and Mass Transfer*, Vol. 15, No. 2, 1972, pp. 301–314. [https://doi.org/10.1016/0017-9310\(72\)90076-2](https://doi.org/10.1016/0017-9310(72)90076-2)
- [42] Coleman, H. W., and Steele, W. G., *Experimentation, Validation, and Uncertainty Analysis for Engineers*, Wiley, Hoboken, NJ, 2009, Chap. 2.

J. Larsson  
Associate Editor